Journal Pre-proof

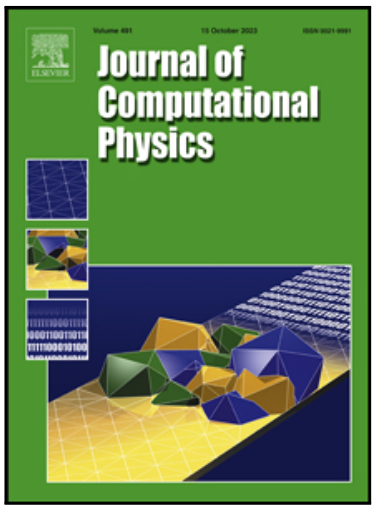

A cluster analysis-based shock wave pattern recognition method for two-dimensional inviscid compressible flows

Siyuan Chang , Jun Liu , Kai Cui

PII: S0021-9991(24)00195-5
DOI: https://doi.org/10.1016/j.jcp.2024.112946
Reference: YJCPH 112946

To appear in: *Journal of Computational Physics*

Received date: 15 August 2023
Revised date: 30 January 2024
Accepted date: 14 March 2024

Please cite this article as: Siyuan Chang , Jun Liu , Kai Cui , A cluster analysis-based shock wave pattern recognition method for two-dimensional inviscid compressible flows, *Journal of Computational Physics* (2024), doi: https://doi.org/10.1016/j.jcp.2024.112946

A cluster analysis-based shock wave pattern recognition method for two-dimensional inviscid compressible flows

Siyuan Chang[a,*], Jun Liu[b], Kai Cui[a,c]

[a]*State Key Laboratory of High-Temperature Gas Dynamics, Institute of Mechanics, Chinese Academy of Sciences, Beijing 100190, PR China*

[b]*School of Aeronautics and Astronautics, Dalian University of Technology, Dalian 116024, PR China*

[c]*School of Engineering Science, University of Chinese Academy of Sciences, Beijing 100049, PR China*

Abstract

Compressible flows typically exhibit multiple shock waves which interact with each other, making the detection of these shock waves crucial for various aspects of flow studies including construction of high-order numerical schemes (e.g., shock-fitting), adaptive grid refinement, and flow visualization. This study aims to effectively identify and localize multiple shock waves and their interaction points in two-dimensional inviscid steady and unsteady flows. A novel shock wave pattern recognition method based on cluster analysis is proposed, including three processes. First, a series of grid-cells located at the transition zones of captured shock waves are extracted using a shock wave detection approach based on local flow variation. Subsequently, these grid-cells are grouped into numerous clusters using the classical *K*-means clustering algorithm, with categorization based on nearest neighbor features. Finally, a strategy is introduced to merge relevant adjacent clusters and further localize the points where shock waves interact. The Bézier curve fitting technique is then employed to obtain the high-quality shock-lines. Several numerical cases demonstrate that this method achieves high localization accuracy for shock-lines while being minimally affected by grid type and scale variations. Moreover, it enables clear and effective identification of the shock interaction patterns in both steady and unsteady flows, providing an effective visualization means for analyzing the motion and evolution of shock wave configurations.

Keywords: shock wave detection; shock-capturing; cluster analysis; shock interactions; compressible flows; unsteady flows

*Corresponding author.

E-*mail addresses*: changsiyuan@imech.ac.cn (Siyuan Chang), liujun65@dlut.edu.cn (Jun Liu), kcui@imech.ac.cn (Kai Cui).

1. Introduction

Shock wave detection poses a formidable challenge in the realm of computational fluid dynamics (CFD). As a strong discontinuity phenomenon within compressible flow fields, shock waves were initially approximated to be situated at the confluence region of flow variable iso-contours during early stages of flow field observation and visualization [1]. However, for complex multi-wave interaction scenarios involving contact discontinuities, expansion waves, and vigorous vortices, this empirical approach is susceptible to misidentifying shock waves. Therefore, it is imperative to develop more accurate shock wave detection techniques.

Since the 1980s, numerous scholars have proposed various methodologies for detecting shock waves based on the computed flow field solutions obtained using shock-capturing methods. In 1985, Buning and Steger [2] suggested that iso-surfaces with a Mach number equal to one along the shock wave normal direction (approximately replaced by a pressure gradient direction) can be considered as shock wave surfaces. This approach was subsequently referred to as the shock wave detection method based on the normal Mach number [3], and gradually gained widespread application in flow visualization. Later, Liou et al. [4] introduced three filtering techniques to eliminate pseudo-shock waves; subsequently, Lovely and Haimes [5] successfully extended this method to detect moving shock waves in unsteady flows. In 1992, Pagendarm and Seitz [6] presented a special method for identifying shock waves based on directional derivatives of flow field density, specifically considering iso-surfaces with second-order directional derivative of density equaling zero as the shock wave fronts, while filtering noise according to first-order directional derivative of density. In 1995, Van Rosendale [7] proposed a shock wave front fitting algorithm for two-dimensional unstructured grids, which aligns grid edges with shock-lines by comparing density gradients between grid-nodes. Then, Ma et al. [8] argued that the local weighting strategy of density gradient in this algorithm could be employed to identify the grid-nodes near shock waves but may require coupling with other flow features for more accurate identification. In 2011, Kanamori and Suzuki [9] applied the theory of characteristics to detect shock-lines and successfully extended it to encompass unsteady and three-dimensional flows [10]. This algorithm, although more intricate compared to the previous methods, obviates the need for empirical threshold parameters in filtering pseudo-shock waves. In 2013, Wu et al. [1] critically reviewed these conventional shock wave detection methods and highlighted that accurately identifying moving and weak shock waves poses a challenging research direction.

In recent decades, artificial intelligence has emerged as a novel research paradigm for advancing fluid mechanics, with the application of machine learning algorithms in shock wave detection gaining significant attention. Some researchers [11-15] have explored the integration of convolutional neural networks into flow visualization to enhance the accuracy and efficiency of shock wave detection. These approaches rely on large-scale training data generated from conventional shock wave detection methods. Additionally, advancements in image edge extraction algorithms have led to the proposal of various two-dimensional shock wave detection techniques

[16-19] that effectively process numerical or experimental schlieren/shadowgraph images. For instance, in 2017, Akhlaghi et al. [17] introduced a novel shock wave detection method by analyzing the Gaussian distribution of flow parameters within numerical schlieren diagrams, which can be effectively applied to both continuous and rarefied flows.

In general, the aforementioned shock wave detection methods are predominantly based on 'local' criteria [20], such as analyzing the local gradients of pressure or density. This implies that the identification of shock wave locations is accomplished by only examining flow parameters within a local grid-node/cell (at most one layer of neighboring grids). However, these detection techniques have inherent limitations and shortcomings due to their focus on local features. On the one hand, they often mistakenly identify scattered data points or small line segments as shock wave fronts due to numerical dissipation and oscillation, resulting in noise, pseudo-shock branches, or gaps appearing on these fronts. On the other hand, these methods offer limited insights into shock wave patterns, such as regular/Mach shock interactions and shock-wall reflection. Consequently, it becomes challenging for these methods to automatically determine both the presence and approximate location of shock interaction points in the flow field.

Recently, the shock-fitting (or shock-tracking) techniques [21-25] have been developed for unstructured or structured grids to address several limitations of mainstream shock-capturing methods in solving two-dimensional compressible flows. In order to explicitly solve Rankine-Hugoniot jump conditions across shock waves, shock-fitting methods typically require information such as the locations of shock waves and shock interaction patterns from the initial shock-capturing solutions. However, without manual intervention or priori knowledge, these aforementioned shock wave detection methods are challenging to directly implement during the initialization of shock-fitting methods, which significantly restricts the application of shock-fitting methods to complex flows.

To address the aforementioned issue, Paciorri and Bonfiglioli [20] introduced an accurate detection method for shock waves and shock interactions in two-dimensional shock-capturing solutions, which can be effectively utilized in the shock-fitting methods [24,25]. Specifically, the initial step involves extracting points within shock wave regions using a conventional shock wave detection method [8], Subsequently, employing the Hough transform technique enables searching for characteristic straight lines among these points while eliminating noise points. The least squares method is then utilized to obtain the curves representing the shock waves. Finally, a fuzzy logic algorithm is applied to identify the shock wave patterns. However, this method exhibits some complexity during implementation and may occasionally misjudge short-length shock wave branches; moreover, its applicability to three-dimensional and unsteady flows remains challenging.

In this paper, we propose a straightforward two-dimensional shock wave pattern recognition method based on cluster analysis, which is comprehensively described by integrating a steady flow example in Sect. 2. In Sect. 3, the accuracy and effectiveness of this method are demonstrated through various steady and unsteady compressible flow test cases. Finally, the research conclusions and future prospects are summarized in Sect. 4.

2. Two-dimensional shock wave pattern recognition method

The novel two-dimensional shock wave pattern recognition method is exemplified through its application to a steady, inviscid shock reflection problem as described in [20]. Fig. 1 shows the geometry of computation domain, boundary conditions, and the entire density field computed using the shock-capturing solver introduced in [26]. In this example, the uniform free-stream Mach number is $M_\infty = 1.5$, and a $10°$ ramp with height of $0.17L$ exists at the lower slide wall of the two-dimensional duct. The oblique shock arising from the concave corner undergoes Mach reflection at the upper slide wall, subsequently interacting with an expansion wave induced at the convex corner of the lower wall before undergoing regular reflection on the lower slide wall. Although this solution was computed on uniform triangular grid-cells, it should be noted that the present method can be applied to any type of grid-cell. The specific implementation process of this method will be successively introduced in the following three subsections.

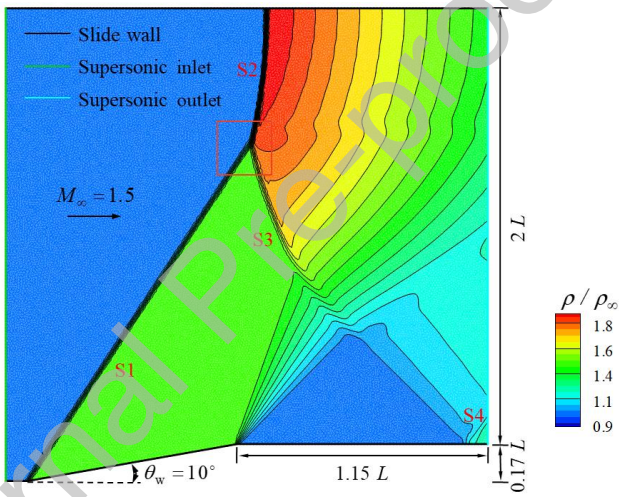

Fig. 1. Shock reflection in a two-dimensional duct: computational domain, boundary conditions, and density iso-contours

2. 1. Identification of shock-cells

Fundamentally, the present method is implemented on the grid-cells rather than the grid-points utilized in [20]. Initially, a three-step procedure is employed to identify a shock-cell cloud, which characterizes the locations of shock waves in the grid-cells, by utilizing a local density gradient-based shock wave detection at each grid-cell center within the shock-capturing solution.

(i) The component of density gradient $\nabla\rho$ along the flow velocity vector $\boldsymbol{v}$ is calculated for all grid-cells in the entire numerical domain:

$$\delta\rho = \frac{\boldsymbol{v}}{\|\boldsymbol{v}\|} \cdot \nabla\rho \tag{1}$$

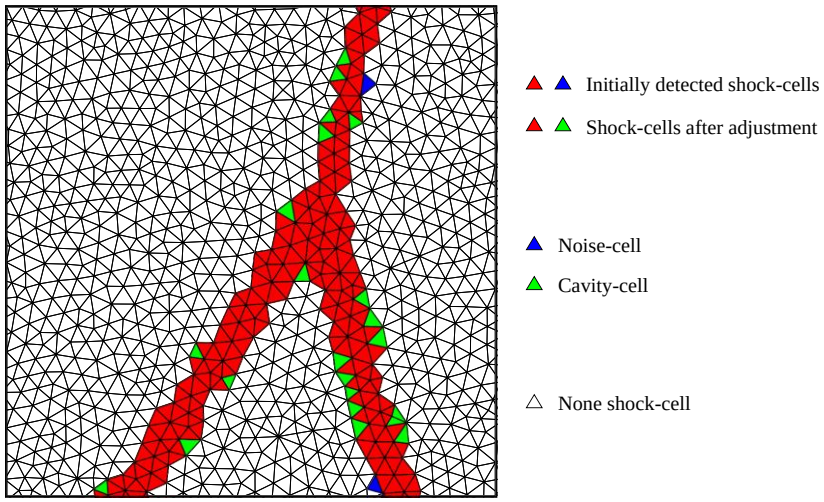

Fig. 2. Initially detected shock-cells near the triple point and corresponding adjustment process (the reader is referred to the web color version of this article)

Due to the consideration of local flow directions, the positive and negative signs of $\delta\rho$ correspond to the fluid being compressed and expanded, respectively. The flow through the shock wave experiences significant compressibility. Therefore, in order to eliminate regions with negligible density gradients, we have devised the following filtering criterion:

$$\delta\rho < \xi_1 \tag{2}$$

where ξ_1 is the filtering threshold parameter that should be set to a 'small' positive value. After conducting numerous numerical case tests, we recommend $\xi_1 = 0.5$ as the default value.

(ii) For most flow fields, the identified shock-cell cloud can generally be obtained after step (i). Moreover, in order to enhance the method's universality to some extent, the grid-cells satisfying Eq. (3) are further eliminated:

$$\delta\rho < \xi_2 \delta\rho_{\max}^{n} \ \&\& \ \delta\rho < \xi_3 \tag{3}$$

where && represents logical conjunction, ξ_2 and ξ_3 are the local filtering threshold parameters, $\delta\rho_{\max}^{n}$ denotes the local maximum value of $\delta\rho$, and the superscript n determines the range of self-defined local regions for each grid-cell. Specifically, for a grid-cell, its local region encompasses the surrounding n-layer grid-cells including itself. In this study, we recommend setting $\xi_2 = 0.4$, $\xi_3 = 2.0$, and $n = 10$ as the initial threshold parameters.

(iii) The initially detected shock-bands, composed of numerous shock-cells (marked in red and blue) near the triple point of Mach reflection, are illustrated in Fig. 2. It should be noted that the presence of various noises and cavities at the edges of shock-bands is attributed to numerical errors arising from shock-capturing processes. To enhance the accuracy and reliability of subsequent cluster analysis results, an optimization process for initial shock-bands is conducted through two successive steps: first, the cavity-cells are added as the new shock-cells; second, the noise-cells are eliminated. Specifically, a cavity-cell (indicated by the green grid-cell in Fig. 2) refers to a non-initially detected shock-cell with all its grid-nodes located on

the initial shock-band; whereas a noise-cell (depicted by the blue grid-cell in Fig. 2) represents an initially detected shock-cell having less than two adjacent co-edge shock-cells.

Certainly, while we employ the conventional shock wave detection method described in step (i) to obtain the shock-cell cloud shown in Fig. 2, alternative detection methods discussed in [1] can be utilized instead. Note that by utilizing the local shock wave detection criterion outlined in step (ii), the mid-lines of those detected shock-bands align more closely with the actual locations of shock waves. Furthermore, despite the clear revelation of three shock waves through the displayed shock-cells in Fig. 2, automatically identifying accurate shock interaction patterns and determining the location of triple point remains challenging. In the subsequent subsections, we will describe how it becomes feasible to automatically extract the shock-lines and recognize the accurate shock interaction patterns through post-processing of the detected shock-cell cloud.

2. 2. Cluster analysis of shock-cells

In this section, we will employ the cluster analysis technique to identify the spatial points featuring the positions of shock waves based on the detected shock-cells.

2. 2. 1. K-means clustering algorithm

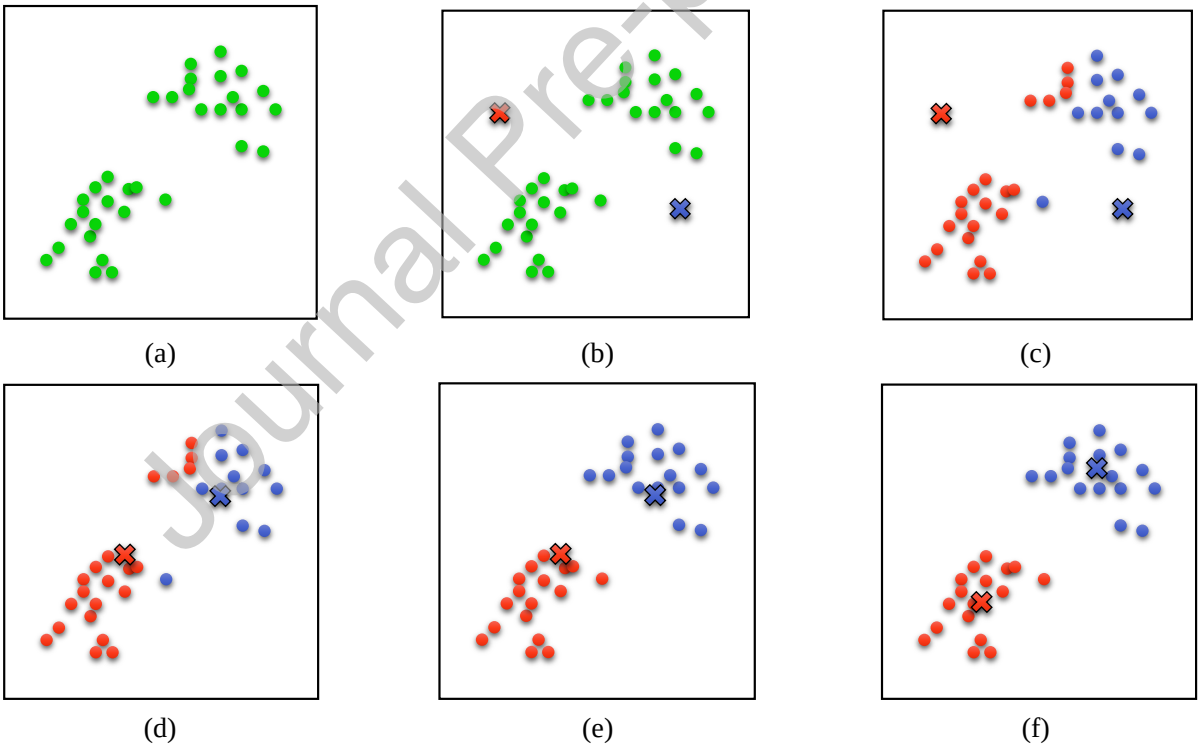

Fig. 3. Schematic diagram of *K*-means clustering algorithm: (a) a dataset, (b) initial cluster centers, (c) 1st clustering process, (d) update cluster centers, (e) 2nd clustering process, (f) final cluster centers (the reader is referred to the web color version of this article)

Cluster analysis is a generic term for a wide range of numerical methods with the common goal of discovering groups (or clusters) of observations that are homogeneous and separated from

other groups [27]. The K-means clustering algorithm [28], which has been developed for over five decades, is one of the most widely-used clustering algorithms in diverse fields. In this section, we provide a concise description of the procedures involved in the K-means clustering algorithm through an illustrative example depicted in Fig. 3.

Let $Q = \{q_i \mid i = 1, 2, \ldots, N\}$ be a dataset consisting of N samples, as shown in Fig. 3(a), and let $X = \{x_i \mid i = 1, 2, \ldots, K\}$ denote a set of K cluster center positions. Moreover, the set of samples belonging to the kth cluster can be defined as:

$$S_k = \{q_j \mid j = 1, 2, \ldots, M_k\}, \quad k = 1, 2, \ldots, K \tag{4}$$

where M_k represents the number of samples in the kth cluster. The iterative calculation of cluster centers for the K-means clustering algorithm proceeds as follows:

(i) The positions of initial cluster centers, denoted as X, can be determined by employing random sampling or other appropriate strategies. As illustrated in Fig. 3(b), two initial cluster centers ($K = 2$) are represented by red and blue X-shaped markers.

(ii) The membership of each cluster is determined based on the criterion of minimum distance from the cluster centers. In Fig. 3(c), following the first clustering process, all samples are partitioned into two clusters marked by red and blue. It is worth noting that there are various algorithms for calculating the distance indicators. In this paper, we adopt the widely-used Euclidean distance to minimize the following cost function defined as follows:

$$\Omega = \sum_{i=1}^{N} dis(q_i, x_k) \tag{5}$$

where $dis(q_i, x_k)$ measures the Euclidean distance between a sample q_i and its corresponding cluster center x_k.

(iii) Update all the cluster centers as follows:

$$x_k = \frac{\sum_{q_j \in S_k} q_j}{M_k} \tag{6}$$

The two new cluster centers after the update are illustrated in Fig. 3(d).

(iv) Repeat steps (ii) and (iii) iteratively until convergence, where no further changes occur in all cluster centers. The final cluster centers obtained after the second clustering process, as shown in Fig. 3(e), are presented in Fig. 3(f).

2. 2. 2. Cluster center initialization algorithm for shock-cells

The K-means clustering algorithm can be easily implemented, efficiently handling large datasets and converging rapidly. However, in iterative clustering algorithms, the initial positioning of the cluster centers typically plays a crucial role in determining the final clusters [29]. In other words, randomly chosen initial cluster centers may lead to suboptimal results when employing the K-means clustering algorithm. Therefore, when clustering the shock-cells, it is crucial to carefully select the initial cluster centers, ensuring they are neither excessively distant from the shock-bands

nor overly concentrated or sparse in distribution. The initialization strategy for cluster center selection in shock-cells clustering is presented as follows:

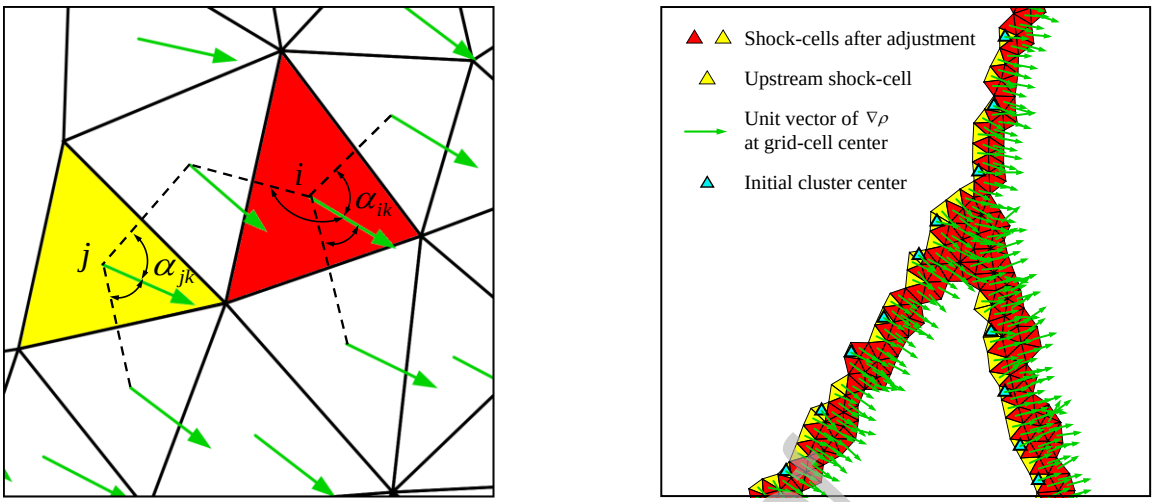

(a) (b)

Fig. 4. Initialization of cluster center for shock-cells: (a) schematic diagram of cluster center initialization algorithm for shock-cells, (b) upstream shock-cells and initial cluster centers within the region surrounding the triple point (the reader is referred to the web color version of this article)

(i) The angles α_{ik} for a shock-cell i, indicated by the red triangle in Fig. 4(a), is computed as follows:

$$\alpha_{ik} = \mathrm{Ang}(\nabla\rho_i, \boldsymbol{x}_k - \boldsymbol{x}_i) \tag{7}$$

where $\nabla\rho_i$ represents the density gradient vector at the cell center, marked by a green arrow; $\boldsymbol{x}_i$ is the center coordinate of shock-cell i, and $\boldsymbol{x}_k$ denotes the center coordinate of the kth adjacent shock-cell. Note that α_{ik} has a range of $[0°, 180°]$.

(ii) Let f_i be the number of satisfying the relation $\alpha_{ik} > 91°$, and let m_i be the total number of co-edge adjacent shock-cells for shock-cell i (e.g., $m_i = 3$ for triangle shock-cells in Fig. 4). Therefore, the parameter f_i, constrained by $0 \le f_i \le m_i$, can approximately indicate the position of shock-cells on the shock-bands:

$$f_i = \begin{cases} 0, & \text{if shock} - \text{cells approach the upstream region} \\ m_i, & \text{if shock} - \text{cells approach the downstream region} \\ (0, m_i), & \text{if shock} - \text{cells approach the middle of shock} - \text{bands} \end{cases} \tag{8}$$

Subsequently, the shock-cell satisfying $f_i = 0$ can be referred to as the 'upstream shock-cell'. Fig. 4(b) clearly illustrates the upstream shock-cells (highlighted in yellow) present on the shock-bands near the triple point.

(iii) All the centers of upstream shock-cells can be considered as the candidates of the initial cluster center. However, in most cases, the distribution of upstream shock-cells is excessively dense, as clearly shown in Fig. 4(b). Therefore, a removal procedure is necessary to obtain initial

cluster centers with a reasonable number and distribution. More specifically, for an upstream shock-cell i, the other upstream shock-cells whose corresponding center distances satisfying Eq. (9) are eliminated.

$$\|\boldsymbol{x}_i - \boldsymbol{x}_j\| < \eta L_i \tag{9}$$

where $\boldsymbol{x}_i$ and $\boldsymbol{x}_j$ are the center coordinates of the upstream shock-cell i and the other upstream shock-cell j, respectively. η represents the spacing coefficient that controls the distances between initial cluster centers, and we suggest $\eta = 3$ in most cases. L_i is the local grid size for the upstream shock-cell i, which is computed using Eq. (10).

$$L_i = \frac{\sum_{k=1}^{n_i} \|\boldsymbol{x}_i - \boldsymbol{x}_k\|}{n_i} \tag{10}$$

where n_i is the total number of co-edge adjacent grid-cells for the shock-cell i, $\boldsymbol{x}_i$ and $\boldsymbol{x}_k$ represent the center coordinates of the shock-cell i and its kth adjacent grid-cell, respectively. It should be noted that the local grid size parameter L_i establishes a positive correlation between the initial distance of centers and the grid size. Subsequently, repeat this process for all existing upstream shock-cells, and finally we can regard the centers of remaining upstream shock-cells as the initial cluster centers, as indicated by the cyan triangle symbols in Fig. 4(b).

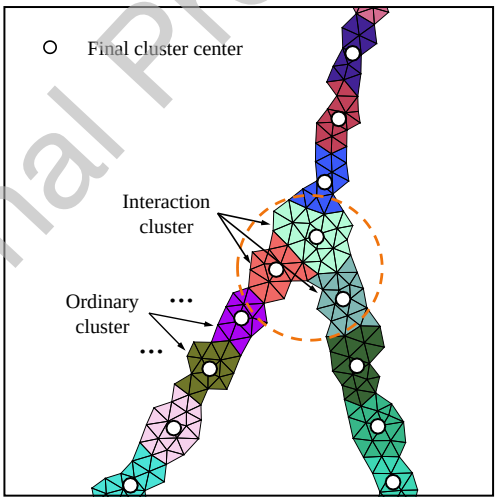

Fig. 5. Result of *K*-means clustering for shock-cells within the region surrounding the triple point, with the spacing coefficient $\eta = 3$ (the reader is referred to the web color version of this article)

After determining the initial cluster centers, all the shock-cell centers can be considered as the dataset to start the *K*-means clustering process introduced in Sect. 2.2.1. Hereafter, we refer to a cluster containing multiple detected shock-cells as a 'shock-cluster'. Fig. 5 illustrates the final shock-clusters and their corresponding cluster centers (marked by white circle symbols) within the region surrounding the triple point. Note that various colors are utilized in this paper to distinguish adjacent shock-clusters effectively.

Further, there are two details that need to be discussed in the aforementioned cluster center initialization algorithm. On the one hand, during the removal procedure (iii), the initial positions of cluster centers indeed change if the center ordering changes, and then the clustering results may also change. However, some numerical experiments indicate that the change of initial center positions is limited (usually to a few local grid scales) even if the center ordering changes. Moreover, the subsequent *K*-means clustering process will further reduce the impact of such changes. In a word, the change of the center ordering has little effect on the result of shock wave pattern recognition. On the other hand, the spacing coefficient η introduced in Eq. (9) has great influence on the recognition result. Both too large and too small values of η can affect the reasonableness of the number and distribution of initial cluster centers, and further cause unexpected issues. For example, if η is too small, such as $\eta = 1$, numerous initial cluster centers can be obtained, resulting in some unreasonable shock-clusters marked by the dashed circle boxes in Fig. 6(a). These unreasonable shock-clusters can further lead to misjudgment of shock wave pattern recognition. In contrast, if η is too large, such as $\eta = 8$, only few initial cluster centers can be obtained as shown in Fig. 6(b), which is not conducive to accurate fitting of curved shock waves (introduced in Sect. 2.3.3). Note that there are no unreasonable shock-clusters if the distance of the initial cluster centers is too large. Thus, after numerous numerical experiments, we recommend $\eta = 3$ as the initial value in most cases.

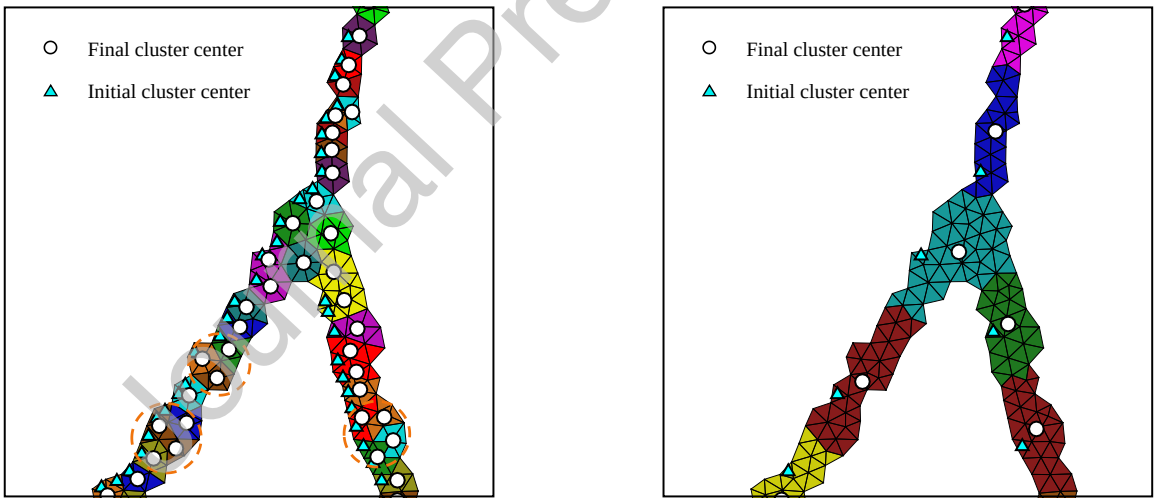

(a) (b)

Fig. 6. Effect of the number of initial cluster centers on clustering results: (a) more initial cluster centers with the spacing coefficient $\eta = 1$, (b) less initial cluster centers with $\eta = 8$ (the reader is referred to the web color version of this article)

2. 3. Pattern recognition of shock waves

2. 3. 1. Classification of shock-clusters

In order to accurately analyze the shock wave patterns in the subsequent procedure, the shock-clusters obtained in Sect. 2.2 are categorized into four groups: ordinary cluster, boundary cluster, interaction cluster, and end cluster, as illustrated in Fig. 7. Each shock-cluster can be classified based on its nearest neighbor features, including location and number of adjacent clusters, as presented in Table 1.

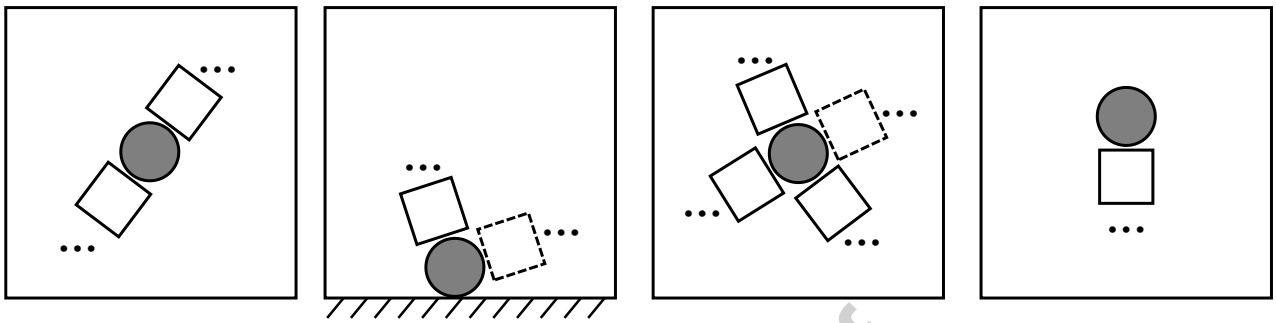

(a) (b) (c) (d)

Fig. 7. Classification diagram of the shock-clusters: (a) ordinary cluster, (b) boundary cluster, (c) interaction cluster, (d) end cluster

1) The ordinary cluster, which is only adjacent to two shock-clusters, represents the most prevalent shock-cluster along shock-lines within the computational domain, as shown in Fig. 5. 2) The end cluster, which is merely adjacent to one shock-cluster, corresponds to the termination of shock-lines within the computational domain. 3) The interaction cluster, which is adjacent to more than two shock-clusters, typically exists in the shock interaction regions within the computational domain. For example, Fig. 5 demonstrates three interaction clusters located in the region surrounding the triple point. 4) The boundary cluster, adjacent to the computational boundary (e.g., inlet, outlet, wall), indicates potential interactions between a shock wave and the computational boundary.

Furthermore, in this paper, the boundary cluster, interaction cluster, and end cluster are collectively referred to as the 'key cluster'. Despite their scarcity, these key clusters are often located at critical positions where significant changes occur in shock wave patterns or shapes. Moreover, they serve as crucial indicators for identifying shock wave patterns as described in Sect. 2.3.2.

Table 1 Four kinds of shock-clusters and corresponding nearest neighbor features

Classification	Location characteristics	Number of adjacent clusters	Frequency of occurrence
Ordinary cluster	Internal field	2	High
Boundary cluster	Adjacent to boundary	$\geq$ 1	Less
Interaction cluster	Internal field	$\geq$ 3	Less
End cluster	Internal field	1	Less

2. 3. 2. Identification of shock wave patterns

The accurate identification of shock wave patterns in the computational domain, particularly the accuracy localization of 'key shock points' such as triple point and regular reflection point, presents a formidable challenge. In this section, we propose a novel methodology for identifying shock wave patterns by conducting further analysis on the shock-clusters.

First, if necessary, merge some adjacent shock-clusters. More specifically, there are two situations that require a cluster merge operation. On the one hand, when the multiple interaction clusters are adjacent to each other as illustrated in Fig. 8(a), they should be merged into a single large cluster as shown in Fig. 8(b). In other words, the shock-cells originally contained in multiple adjacent interaction clusters will collectively belong to the same cluster. On the other hand, merge these adjacent boundary clusters located on the same computational boundary as shown in Fig. 8(a) and 8(d). For example, in the region where the shock-wall regular reflection occurs, we initially observe two adjacent boundary clusters, as displayed in Fig. 9(a). Following the cluster merge operation, a single large cluster emerges, as shown in Fig. 9(b).

Subsequently, it is imperative to reclassify these post-merged clusters based on the criteria described in Sect. 2.3.3 and recalculate their centers using Eq. (6). For example, Fig. 10 demonstrates the amalgamation of three adjacent interaction clusters depicted in Fig. 5, resulting in a new interaction cluster.

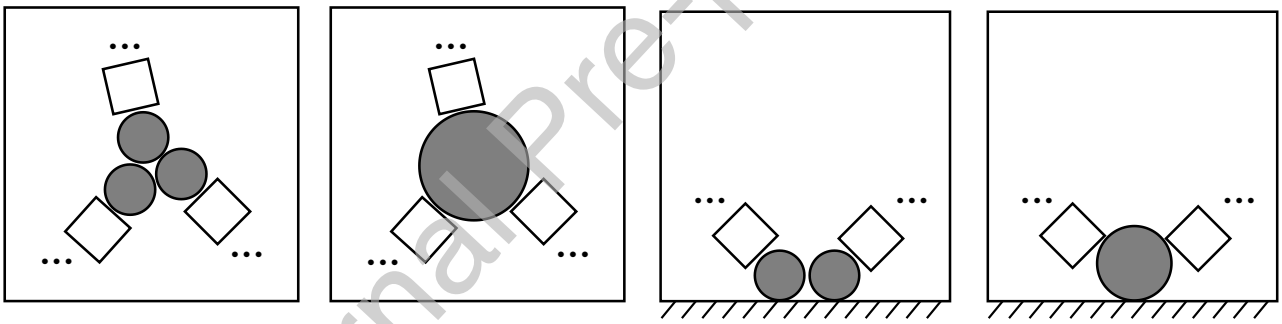

(a) (b) (c) (d)

Fig. 8. Schematic diagram of pre-merge and post-merge for the shock-clusters: (a) pre-merged interaction clusters, (b) post-merged interaction cluster, (c) pre-merged boundary clusters, (d) post-merged boundary cluster

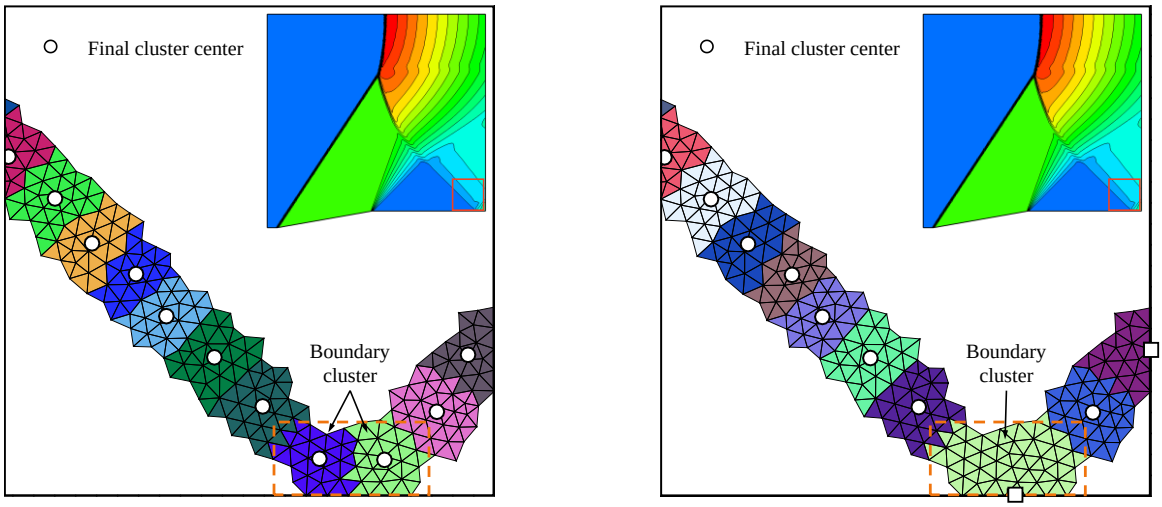

(a) (b)

Fig. 9. Results of shock-clusters within the region where the shock-wall regular reflection occurs: (a) pre-merged, (b) post-merged (the reader is referred to the web color version of this article)

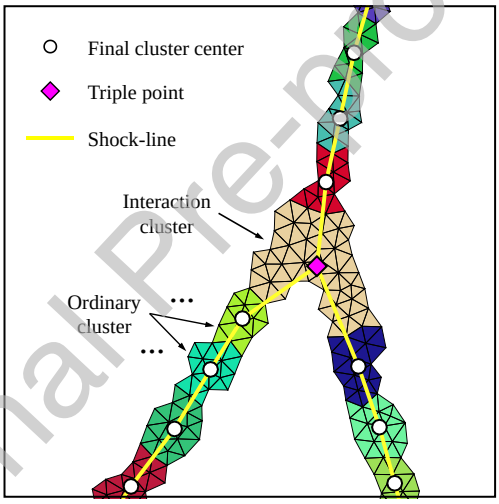

Fig. 10. Post-merged result of shock-clusters within the region surrounding the triple point (the reader is referred to the web color version of this article)

Finally, the clear identification of shock wave patterns is facilitated by the near-neighbor characteristics exhibited by key clusters. Fig. 11 illustrates six distinct shock wave patterns along with their corresponding shock points, while Fig. 12 provides a detail flowchart for identifying these patterns. Specifically, the identification strategy primarily encompasses the following three aspects:

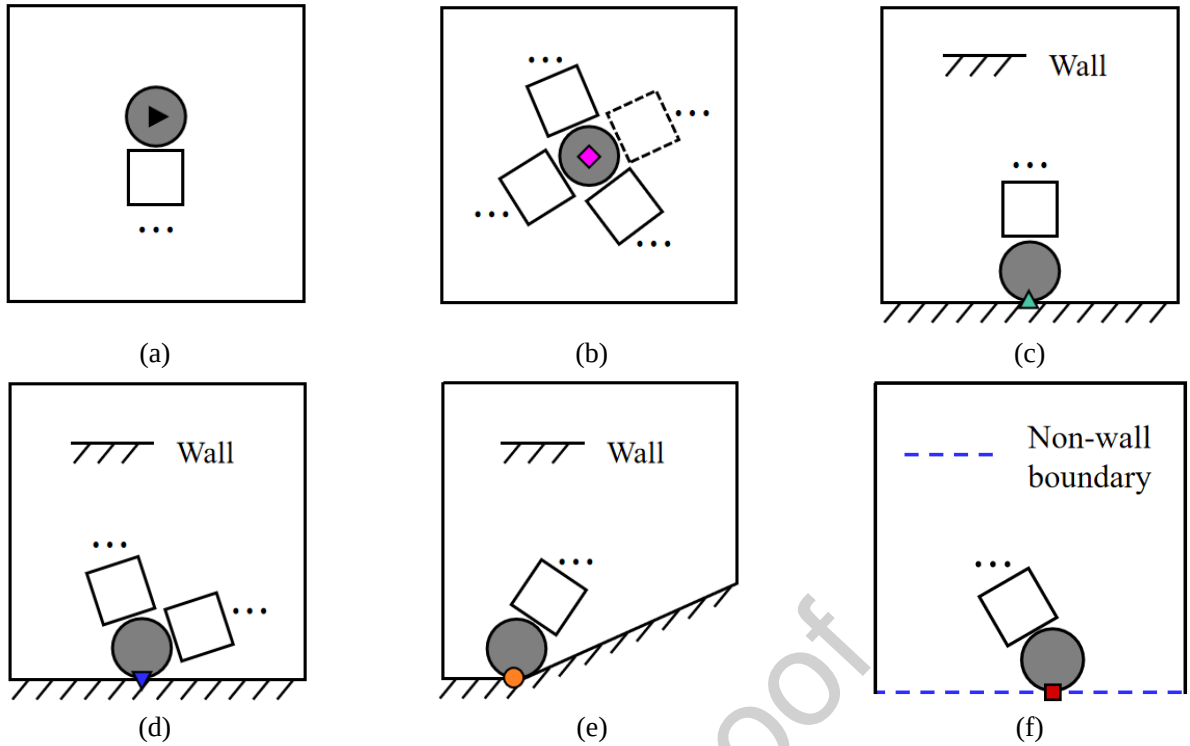

Fig. 11. Classification diagram of shock wave patterns and key shock points: (a) end shock point, (b) triple/quadruple point, (c) normal shock point, (d) regular reflection point, (e) oblique shock point, (f) inlet/outlet point

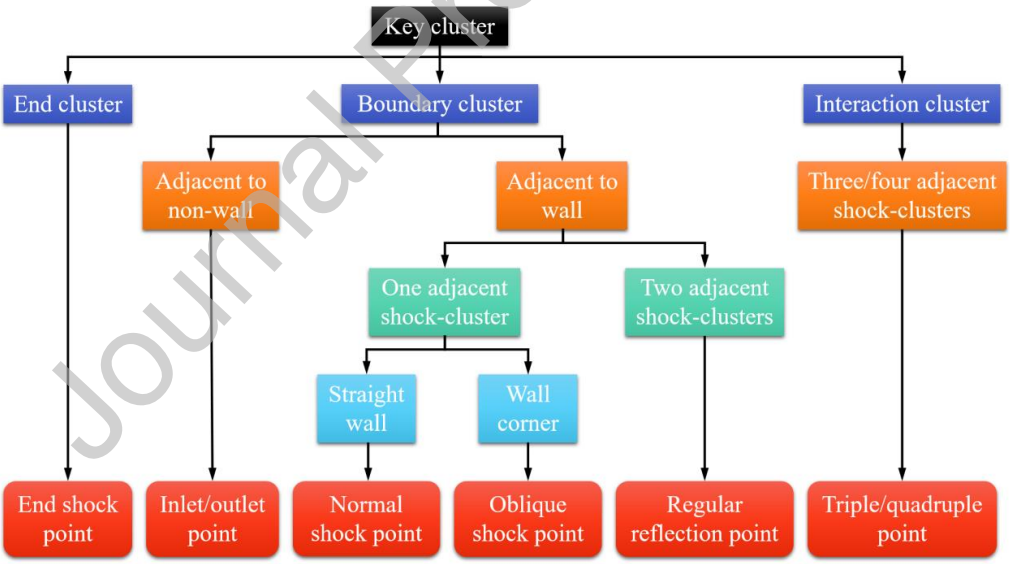

Fig. 12. Flowchart of shock wave pattern identification

(i) For an end cluster, its center can be considered as the termination point of the shock-line, referred to as the end shock point, as shown in Fig. 11(a).

(ii) For an interaction cluster, if it is adjacent to three or four shock-clusters, as depicted in Fig. 11(b), its center can be considered as the triple or quadruple point resulting from shock-shock interactions, respectively.

(iii) For a boundary cluster, four shock wave patterns can be identified based on the number of

adjacent shock-clusters and the condition of adjacent computational boundaries. 1) If a boundary cluster is adjacent to only one cluster and its adjacent boundary is a straight wall, as shown in Fig. 11(c), a normal shock wave occurs off the wall, with the center of the interface between the boundary cluster and straight wall serving as the normal shock point. 2) If a boundary cluster is adjacent to two clusters, as shown in Fig. 11(d), a regular shock reflection occurs; thus, the center of the interface can be considered as the regular reflection point. 3) If a boundary cluster is adjacent to one cluster and a wall corner, as shown in Fig. 11(e), an oblique shock wave may exist where this wall corner can be considered as an oblique shock point. 4) If a boundary cluster adjoins a non-wall boundary (e.g., inlet/outlet or non-reflecting boundary), as illustrated in Fig. 11(f), the shock wave crosses the boundary without reflection; thus, the center of the interface between boundary cluster and non-wall boundary can be considered as the inlet/outlet point.

2. 3. 3. Curve fitting of shock-lines

Upon identification of a two-dimensional shock interaction pattern, individual shock wave branches, referred to as shock-lines, can be further obtained.

First, the shock-clusters corresponding to each shock wave can be easily obtained through the neighbor relationships between shock-clusters. Specifically, initiating the search from an arbitrary key cluster identified in Sect. 2.3.2, sequentially record all the ordinary clusters adjacent to each other along a shock wave branch until reaching another key cluster as termination criteria. Consequently, this sequence of shock-clusters represents a distinct shock wave branch. The search process continues to determine shock-clusters on subsequent shock wave branches until all shock-clusters within the flow field have been iterated.

Then, the shock-lines can be derived by sequentially connecting the corresponding centers of the shock-clusters on each shock wave branch. However, it is worth noting that certain shock-lines may be zigzag, as shown by the solid yellow line in Fig. 10. Therefore, to address this issue comprehensively, we employ the well-known Bézier curve fitting algorithm [30] to effectively smoothen these shock-lines, which will be briefly described below.

For a series of ordered points $\boldsymbol{P}_0, \boldsymbol{P}_1, \ldots, \boldsymbol{P}_n$, the general parameterized form of its *n*th-order Bézier curve can be expressed as follows:

$$\boldsymbol{B}_n(x) = \sum_{i=0}^{n} \frac{n!}{i!\,(n-i)!} \boldsymbol{P}_i (1-x)^{n-i} x^i, \qquad x \in [0,1] \tag{11}$$

where $\boldsymbol{P}_i$ is the control point of the Bézier curve. The curve starts at point $\boldsymbol{P}_0$ (corresponding to $x = 0$) and ends at point $\boldsymbol{P}_n$ (corresponding to $x = 1$). It is worth noting that the Bézier curve exhibits directionality, implying that distinct arrangements of control points yield diverse curves. Moreover, a sufficient and necessary condition for a Bézier curve to be straight lies in the collinearity of all control points.

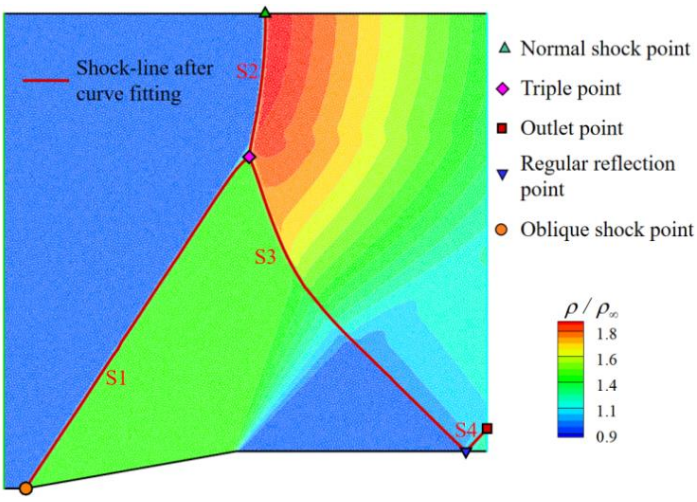

Fig. 13. Curve fitting of shock-lines, key shock points, and density iso-contours in the whole domain

Hence, based on the inherent characteristics of Bézier curves, if a shock wave branch contains $n+1$ shock-clusters, the two key shock points at both ends serve as the initiation and termination points for the Bézier curve, while the centers of the remaining ordinary clusters are sequentially employed as the control points $\boldsymbol{P}_1 \sim \boldsymbol{P}_{n-1}$. Thus, fitting nth-order Bézier curves enables smoother representation of shock-lines

The final detection results are compared with the density iso-contours in Fig. 13, revealing accurate locations of the four fitted shock-lines and five identified key shock points. These results demonstrate the good accuracy of the proposed method and validate the effectiveness of our shock wave pattern recognition strategy.

2. 4. Method summary

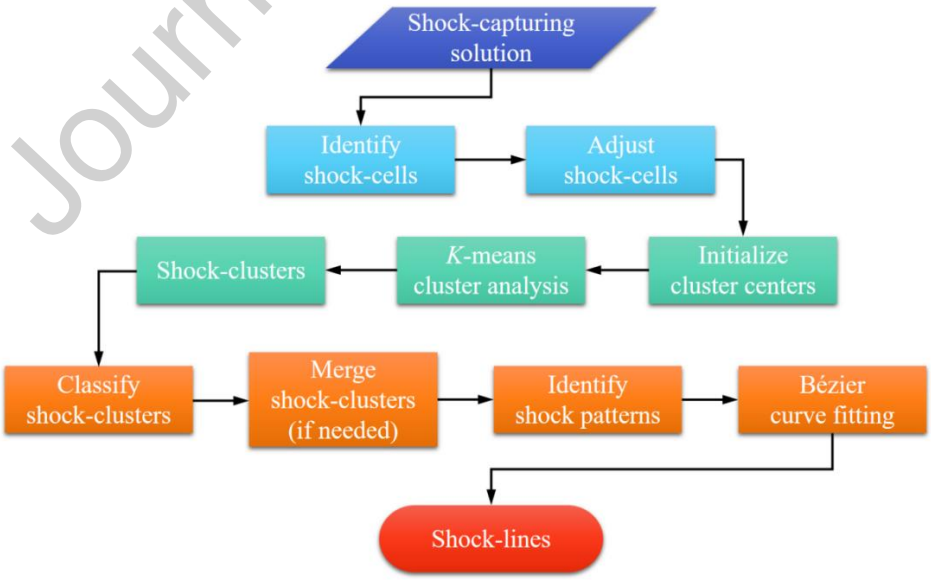

Fig. 14. Flowchart of cluster analysis-based shock detection method

The overall flowchart of this two-dimensional shock wave pattern recognition method is

illustrated in Fig. 14, primarily encompassing three consecutive procedures: shock-cell identification as the fundamental step, cluster analysis as the key component, and pattern recognition as the core element.

Starting from the shock-capturing solution of the two-dimensional inviscid flow filed, the shock-bands with a certain thickness is extracted using a shock wave identification algorithm based on streamwise density gradient projection. Finally, the accurate identification of key positions such as points of shock-shock interaction and shock-boundary interaction is achieved, ensuring high accuracy in both shape and position for each fitted shock-line. Importantly, this method demonstrates minimal dependence on manual intervention while guaranteeing accurate recognition and fitting from the 'shock-band' to the 'shock-line'.

3. Numerical results

The proposed method is validated in this section through four numerical cases of compressible, inviscid flows to verify its accuracy, applicability, and reliability. A second-order cell-centered finite volume framework was employed to solve the two-dimensional Euler equations for calculating the following shock-capturing solutions. Specifically, the inviscid fluxes were solved using the van Leer scheme, and the integration in time was employed using the explicit four-step Runge-Kutta scheme. Previous studies have extensively validated the accuracy and robustness of this shock-capturing solver in various compressible flows [22,26].

3. 1. Hypersonic flow past a semi-cylinder

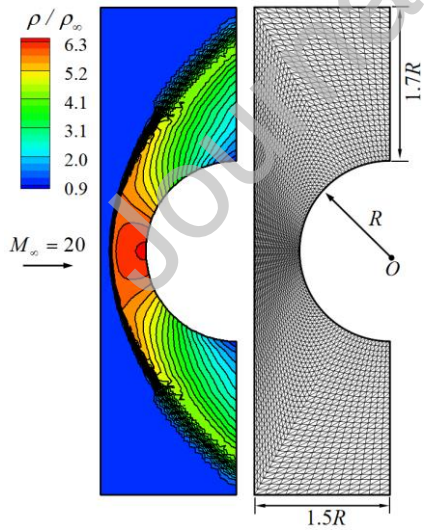

Fig. 15. Hypersonic flow past a semi-cylinder: the computational domain, grid, and density iso-contours

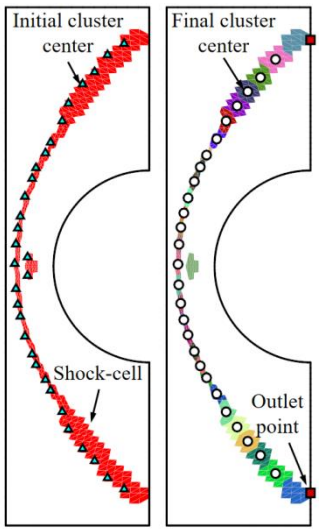

Fig. 16. Hypersonic flow past a semi-cylinder: the detected shock-cells, initial cluster centers, and clustering results

First, a blunt-body flow problem is demonstrated to verify the accuracy of shock-lines detected

using the proposed method. A detached bow shock wave occurs when a uniform hypersonic inflow at Mach number $M_\infty = 20$ passes through a semi-cylinder with a radius of R. Fig. 15 illustrates the computation domain, grid, and density iso-contours of the shock-capturing solution. The computation domain is discretized by 4,800 triangular cells produced by diagonalizing 80(circumferential) × 30(radial) quadrilateral cells. It should be noted that the distribution of grid-cells is non-uniform, with denser grids near the semi-cylinder head and coarser grids near the sides.

The grid-cells located at the bow shock wave position are effectively detected to form a shock-band, as shown in Fig. 16. Obviously, the thickness of this shock-band varies, corresponding to the shock transition zone obtained using the shock-capturing solver. The distribution of initial cluster centers along the shock-band is reasonable, indicating that the initialization algorithm described in Sect. 2.2.2 exhibits good applicability to non-uniform grids. After the cluster analysis, the final cluster centers are located at the middle of the shock-band, and two outlet points on the outlet boundary are also identified, as shown in Fig. 16. Note that although a small shock-band with some spurious shock-cells is detected in the high-pressure zone ahead of the stagnation point due to local high gradients, no shock-lines can be extracted from this shock-band since there are only two corresponding end clusters. This observation highlights the robustness of our method to the small spurious shock wave branches.

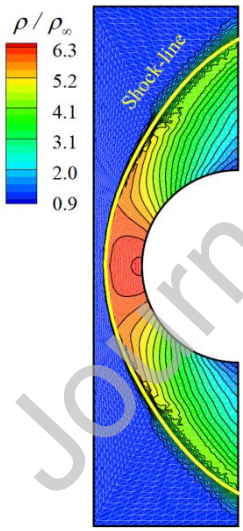

Fig. 17. Hypersonic flow past a semi-cylinder: the comparison between the detected shock-line and the density iso-contours

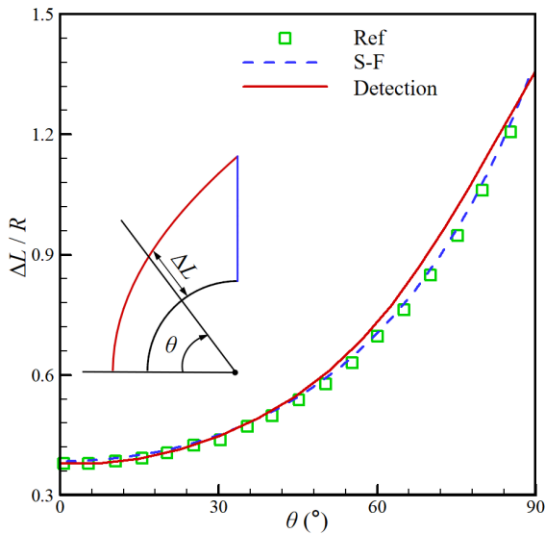

Fig. 18. Hypersonic flow past a semi-cylinder: the comparison of shock-wall distances between Ref. [31], shock-fitting (S-F) solution [23], and detection result

The comparison between the detected shock-line and the density iso-contours, as depicted in Fig. 17, indicates that the shock-line obtained using the curve fitting algorithm in Sect. 2.3.3 is smooth and reasonable. Additionally, Fig. 18 compares the detection results of the shock front positions offset from the semi-cylinder with those from [31] and the shock-fitting solution [23]. The

detection result at polar angle $\theta < 50°$ is accurate and has a small deviation at $\theta > 50°$, suggesting that the grid scale has some influence on the position detection accuracy of bending shock waves. Therefore, enhancing the resolution of captured bending shock waves by refining the grids located at shock wave positions can effectively improve the detection accuracy of curved shock-lines.

3. 2. Shock reflection in a two-dimensional duct

In order to verify the robustness of the proposed method with regard to unstructured grids with large scale variations, we revisit the aforementioned case of shock reflection in a two-dimensional duct introduced in Fig. 1. Differently, the isotropic grid used throughout the entire computational domain in Sect. 2 is changed to an anisotropic grid. As presented in Fig. 19(a), the anisotropic grid is performed along the direction of the incident shock wave, with a height of $0.002L$ for the first layer of grid-cells. Quadrilateral grid-cells are advanced five and ten layers to the left and right sides of the incident shock wave, respectively, with a growth rate of 1.2. Subsequently, the quadrilateral grid-cells on the right side are diagonalized into triangular grid-cells. Moreover, the grid-cells with high aspect ratios near the bottom wall boundary are highlighted in Fig. 19(b). Specifically, the aspect ratio for the first layer of grid-cell is 50. Quadrilateral grid-cells are advanced ten layers with a growth rate of 1.2, after which these cells are diagonalized.

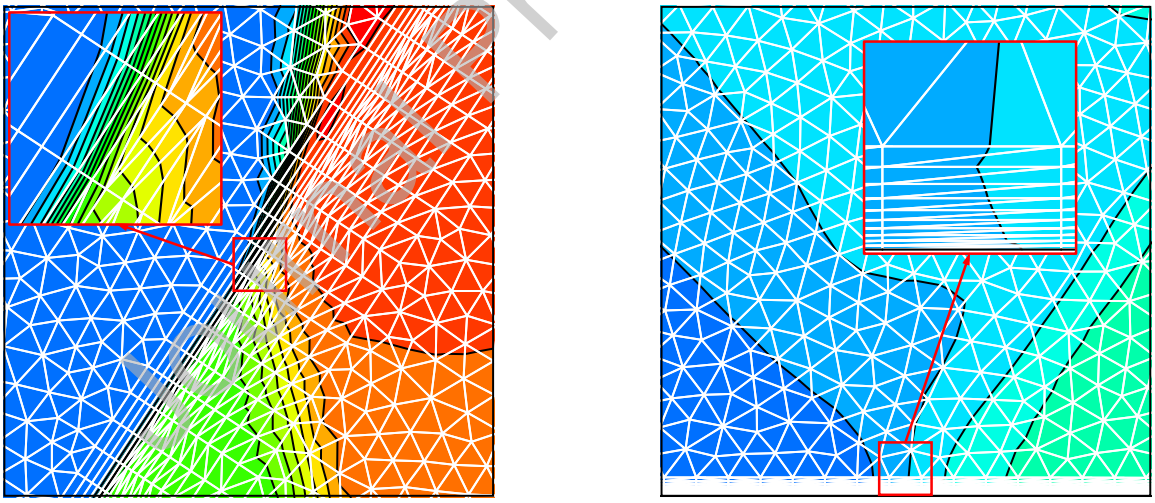

(a) (b)

Fig. 19. Shock reflection in a two-dimensional duct: the background grid and density iso-contours near (a) the triple point and (b) the shock-wall reflection point

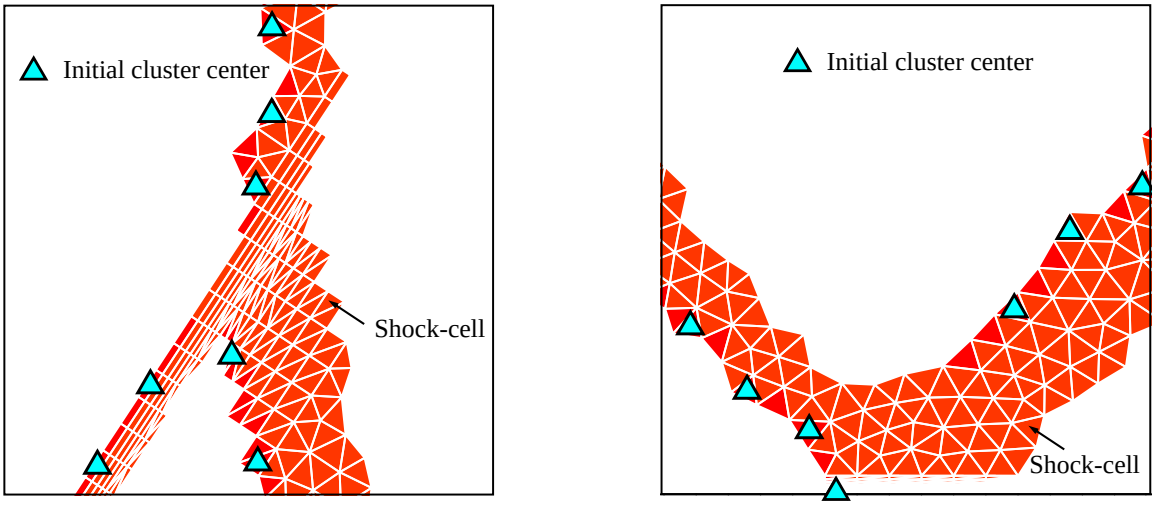

(a) (b)

Fig. 20. Shock reflection in a two-dimensional duct: the shock-cells and the initial cluster centers near (a) the triple point and (b) the shock-wall reflection point

Fig. 20 shows the detected shock-cells and the initial cluster centers. It is evident that despite the significant variation in the thickness of different shock-bands near the triple point, the initial cluster centers are reasonably located and distributed. This demonstrates the effectiveness of the previous cluster center initialization algorithm for anisotropic grids with hybrid types. Similarly, the results in Fig. 20(b) indicate that even when the shock wave spans across grid-cells with high aspect ratios, the initial cluster centers can be effectively obtained. An initial cluster center is located at the refinement region near the wall. Furthermore, Fig. 21 demonstrates the results following *K*-means cluster analysis. Both the interaction cluster and the boundary cluster, which can be used to recognize shock wave patterns, are reasonably identified. It should be noted that an unsuitable initialization of cluster centers tends to yield poor results when using an anisotropic grid in the vicinity of the shock wave interaction zone, as opposed to using an isotropic grid. For instance, the triple point may be located outside the shock-clusters if the initial distance of cluster centers is too large, which could be investigated in the subsequent research.

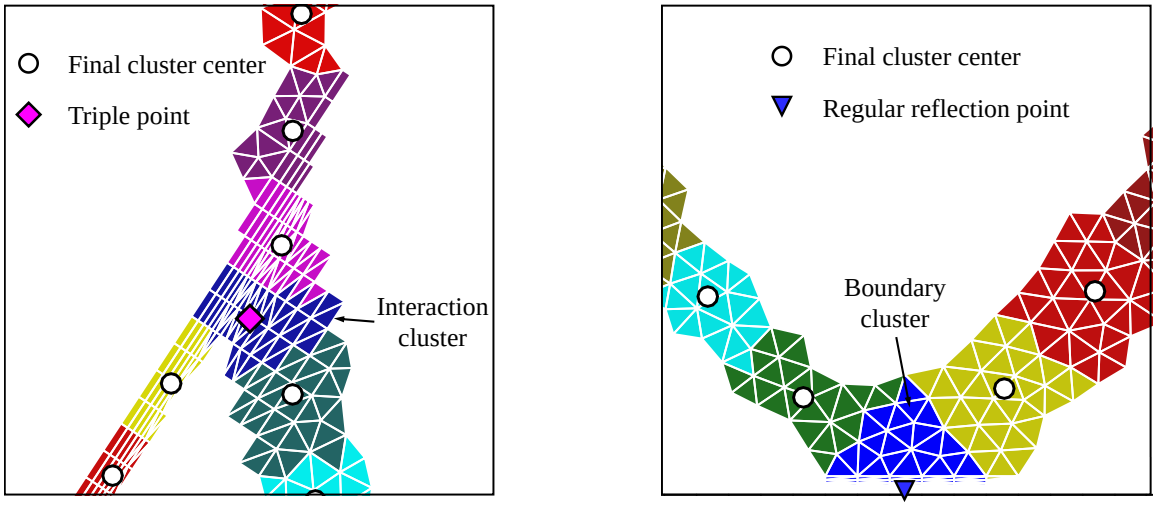

(a) (b)

Fig. 21. Shock reflection in a two-dimensional duct: the clustering results near (a) the triple point and (b) the shock-wall reflection point (the reader is referred to the web color version of this article)

Finally, a comparison of shock-lines under the two aforementioned grid types is presented in Fig. 22. Both the shape and position of the four shock-lines align well with the numerically captured shock waves. As observed in the local enlarged plots, there are slight discrepancies in the positions of the two detected triple points. This discrepancy arises from differences in the initial identification of shock-bands, which poses a challenge to be comprehensively resolved. Fortunately, the deviations are confined to a few local grid scales, which is generally considered acceptable.

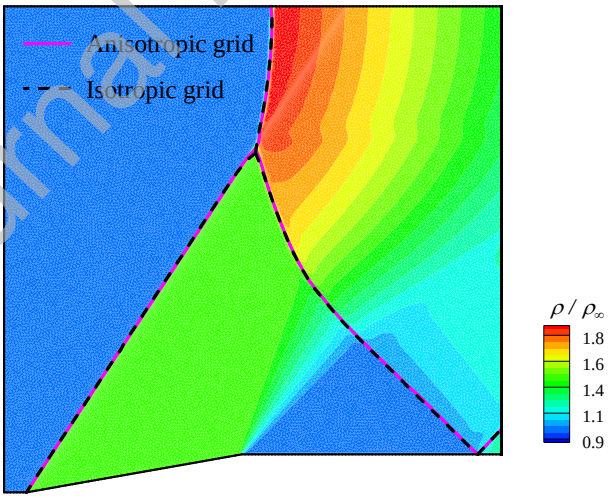

(a)

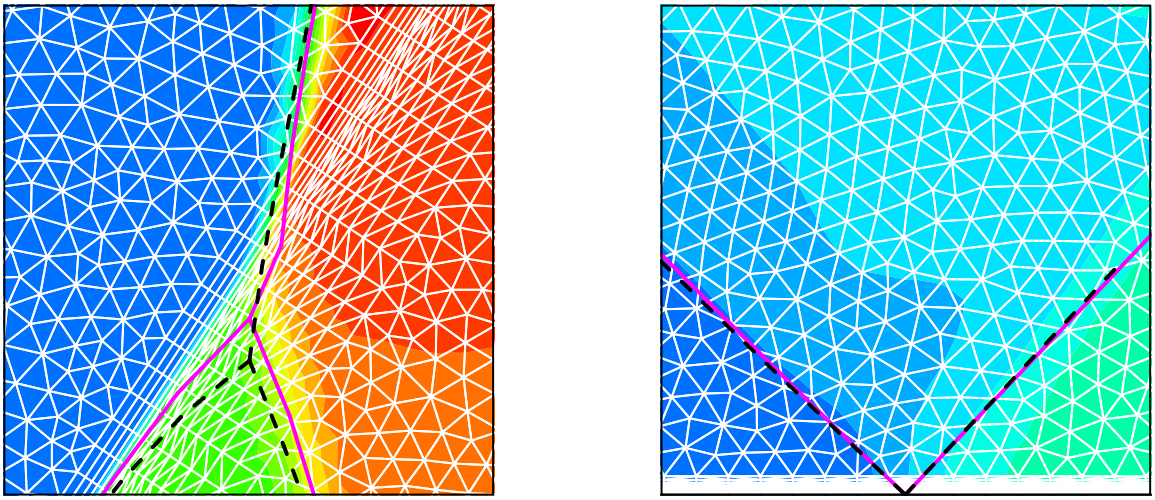

(b) (c)

Fig. 22. Shock reflection in a two-dimensional duct: the comparison results between the detected shock-lines under two grid types and the density iso-contours (a) over the whole computational domain, (b) near the triple point, and (c) near the shock-wall reflection point

3. 3. Supersonic flow over a double-wedge

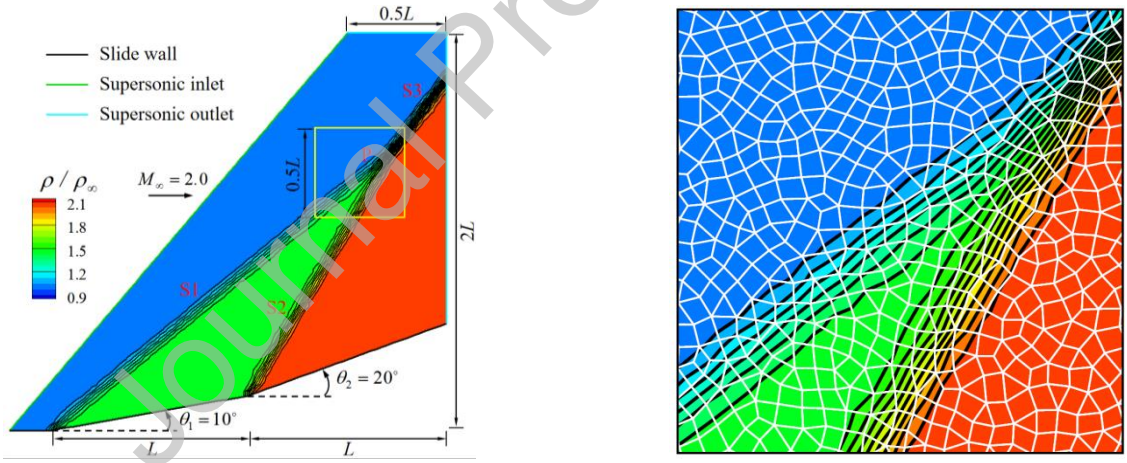

(a) (b)

Fig. 23. Supersonic flow over a double-wedge: (a) the computational domain, boundary conditions, and density iso-contours, (b) the background grid near the shock interaction point

A simulation of inviscid supersonic flow over a double-wedge is presented, featuring an interaction between two shock waves on the same side. Fig. 23(a) illustrates the computational domain, boundary conditions, and density iso-contours. The two wedge surfaces both have a horizontal length of L, with the wedge angles of $\theta_1 = 10°$ and $\theta_2 = 20°$, respectively. A uniform inflow at Mach number $M_\infty = 2$ is successively compressed by both wedge surfaces, generating two oblique shock waves (S1 and S2). Subsequently, these two shock waves undergo a regular interaction and converge into a single shock wave (S3). The entire flow field is discretized using a

uniform hybrid grid consisting of 4,760 cells with an average grid edge length $\Delta = 0.03L$. Fig. 23(b) shows that numerous quadrilateral cells are mixed with some triangular cells near the shock interaction point.

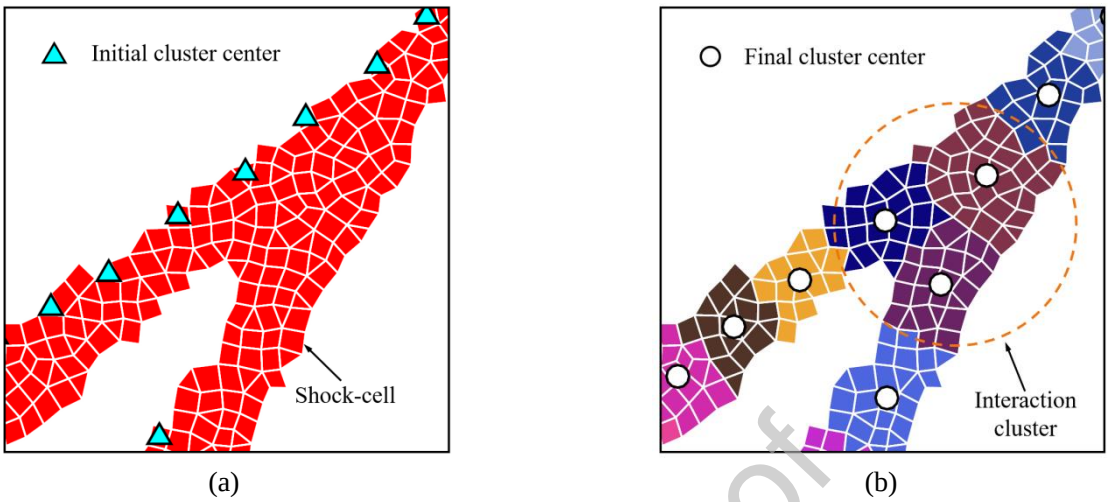

(a) (b)

Fig. 24. Supersonic flow over a double-wedge: (a) the detected shock-cells and initial cluster centers, (b) the clustering results of shock-cells (the reader is referred to the web color version of this article)

The local distributions of detected shock-cells and initial cluster centers are shown in Fig. 24(a), where a significant aggregation of shock-cells is clustered near the shock interaction point. Then, the K-means clustering process is applied to these shock-cells, and the result is depicted in Fig. 24(b). According to the classification criteria for shock-clusters described in Sect. 2.3.1, multiple ordinary clusters are distributed along each shock-band branch, while three interaction clusters congregate proximate to the interaction point. Given their adjacency, it becomes necessary to merge these interaction clusters into a single shock-cluster, as depicted in Fig. 25(a), for further determination of both the shock wave pattern and location of its interaction point.

In fact, the detection accuracy of shock wave locations, especially at shock interaction points, is heavily dependent on flow resolution. In other words, accurately detecting shock wave locations becomes more feasible as the width of the shock transition zone computed using shock-capturing solvers decreases. The impact of grid scale on the detected shock-lines is examined below by creating and utilizing a medium grid ($\Delta = 0.02L$) and a refined grid ($\Delta = 0.01L$) to rerun flow simulations and conduct shock wave pattern recognition. Fig. 25(b) and (c) present the corresponding post-merged results for shock-clusters. As the grid is refined, an increased number of shock-clusters are obtained with reduced spacing between cluster centers, which is determined by the local grid size parameter L_i of Eq. (10) in Sect. 2.2.2.

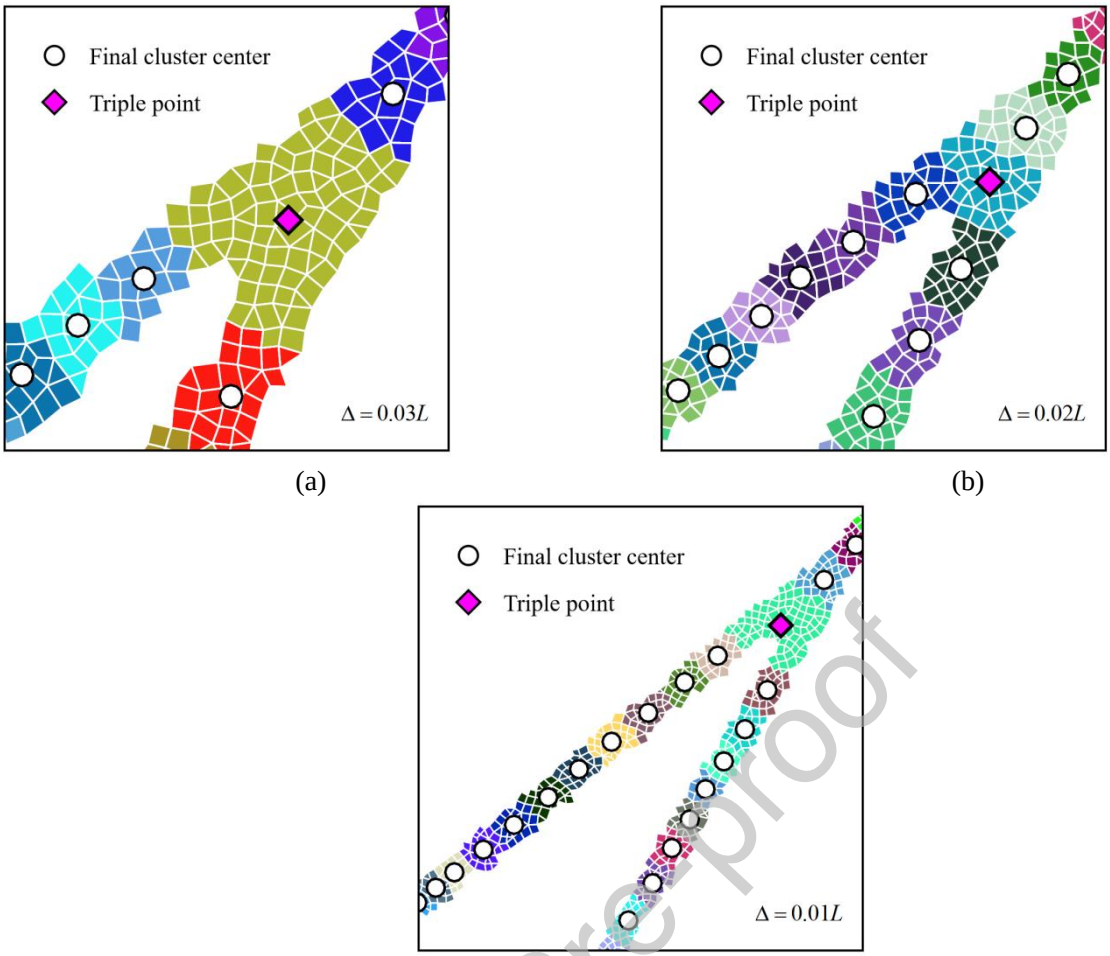

Fig. 25. Supersonic flow over a double-wedge: the post-merged results for shock-clusters obtained on (a) coarse grid, (b) medium grid, and (c) refined grid (the reader is referred to the web color version of this article)

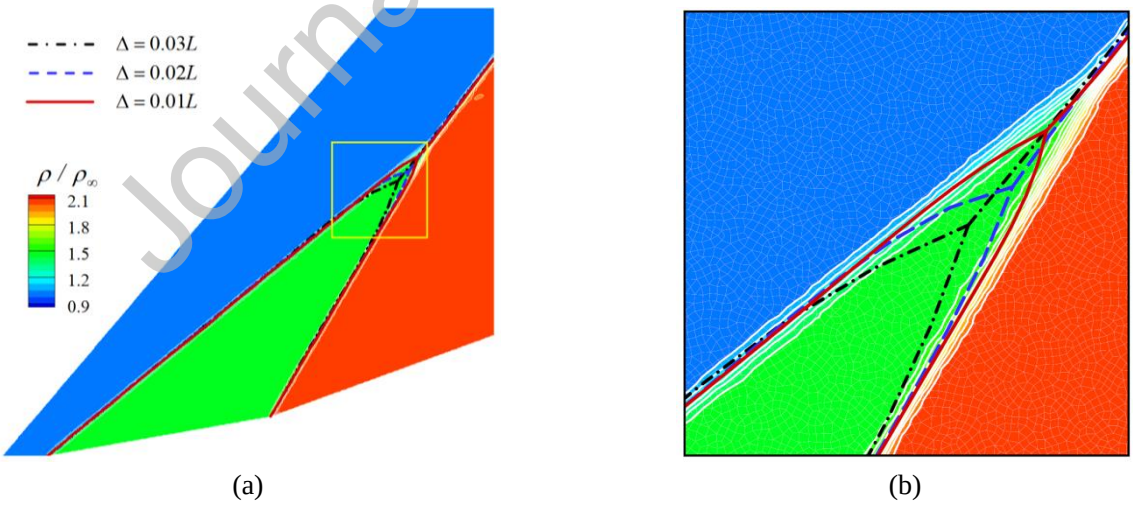

Fig. 26. Supersonic flow over a double-wedge: the comparison between shock-lines detected on three different grid scales (a) over the entire domain and (b) near the shock interaction point

Fig. 26 compares the shock-lines detected on three different grid scales with the density iso-contours obtained on the refined grid, revealing a high level of consistency in most locations.

However, slightly larger discrepancies are observed at the interaction point. This can be attributed to the wider transition zone of captured shock waves when using coarser grids, leading to an early convergence of the two detected shock-bands (as shown in Fig. 25). In brief, this test case demonstrates that the recognition accuracy of the proposed method slightly depends on the grid scale for interaction points formed by shock waves on the same side. However, for straight shock waves located away from these interaction points, the recognition accuracy remains excellent and is minimally affected by variations in the grid scale.

3. 4. Supersonic inlet flow

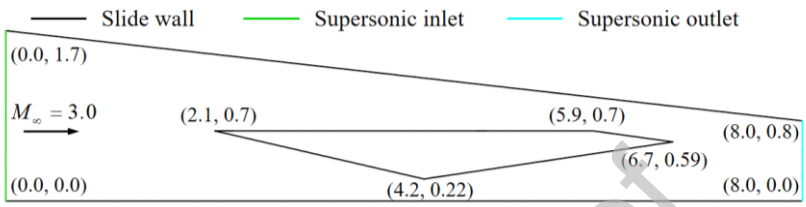

Fig. 27. Supersonic inlet flow: the geometry and boundary condition

Supersonic inlet flows are typical of scramjet engines. The geometry configuration shown in Fig. 27 is referenced from [32], where an inviscid supersonic inflow at Mach number $M_\infty = 3$ enters the engine inlet from the left side. Owing to the unique internal configuration of the inlet, the complex flow characterized by multiple shock wave interactions are expected to appear. To enhance the quality of shock-capturing solutions, an adaptive grid refinement technique is performed. The pressure iso-contours illustrated in Fig. 28 clearly demonstrate the captured complex flow structure on an unstructured grid consisting of 240,338 triangular cells.

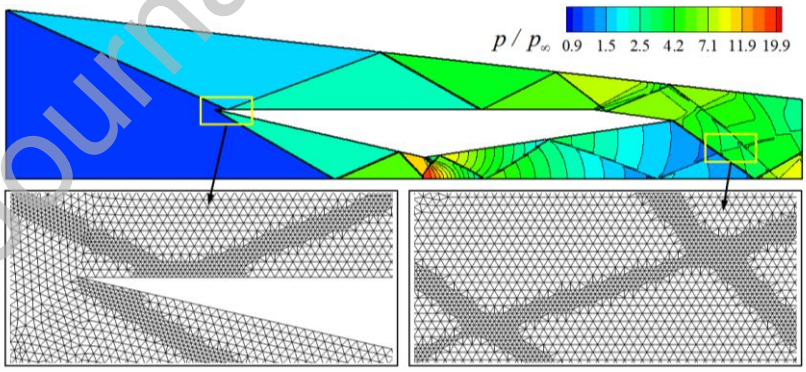

Fig. 28. Supersonic inlet flow: the pressure iso-contours over the entire domain and the adaptively refined grids at the local zones

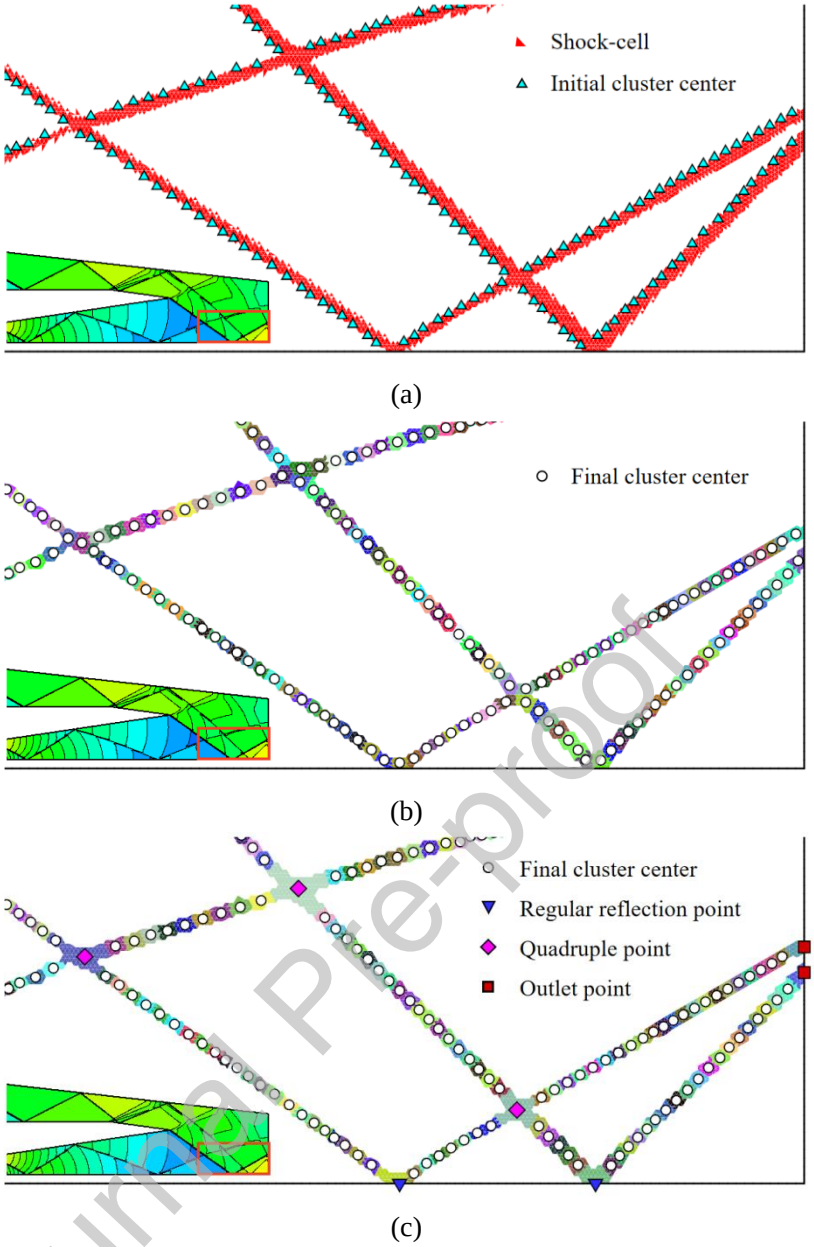

Fig. 29. Supersonic inlet flow: (a) the locally detected shock-cells and the corresponding initial cluster centers, and the (b) pre-merged and (c) post-merged clustering results for local shock-clusters

The detected shock-cells shown in Fig. 29(a) demonstrate the effectiveness of the identification strategy described in Sect. 2.1 for multiple shock waves with varying strengths. The initial cluster centers are appropriately distributed on the upstream side of each shock-band branch. Fig. 29 also presents the pre-merged and post-merged clustering results for shock-clusters near the outlet. Numerous shock-clusters gather at locations where shock-shock and shock-wall interactions occur, and sequential merging of key clusters enables accurate identification of both the type of shock interaction pattern and the locations of interaction points. Fig. 30 compares the detected shock-lines with pressure iso-contours, revealing that all 25 shock wave branches are extracted into smooth shock-lines that align well with captured shock waves. In summary, this case strongly validates the applicability and accuracy of the proposed method in complex shock wave configurations.

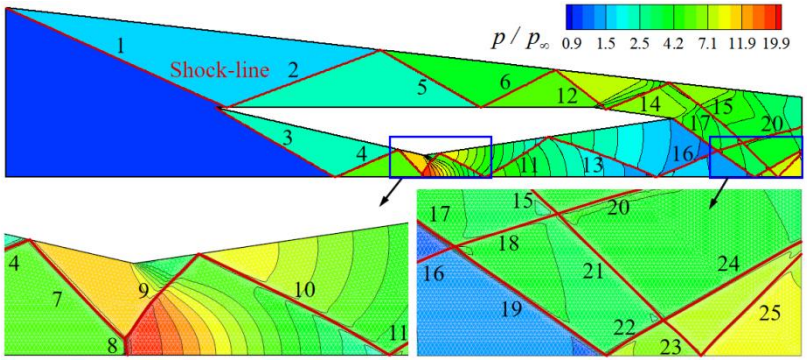

Fig. 30. Supersonic inlet flow: the global and local comparison of the detected shock-lines with the pressure iso-contours

3. 5. Forward-facing step problem

A challenging test for detecting unsteady shock waves involves the numerical simulation of a wind tunnel with a flat forward-facing step, which is commonly used as a standard numerical benchmark to compare various schemes in CFD. The problem under consideration is a Mach 3 flow in a wind tunnel of 1 unit in width and 3 units in length. The forward-facing step is 0.2 units high and it is located at 2.4 units from the right end of the tunnel. Initially, the tunnel is filled with a gas with adiabatic coefficient of 1.4, which everywhere has dimensionless pressure $p = 1$, density $\rho = 1.4$, horizontal velocity $u = 3$, and vertical velocity $v = 0$. An inflow boundary condition is applied at the left end of the computational domain, while an outflow boundary condition is imposed at the right end. Inviscid wall boundary conditions are applied along the walls of the tunnel and on the boundary marked by the step. Furthermore, the entire computational domain is discretized by 54,100 triangular cells with an average grid edge length of 0.01 units; note that the gird is uniform without any special refinement around the corner or at the shock wave positions. The computation terminates at the moment $t = 5$ when a unique and complicated shock wave configuration is formed.

In the evolution of the flows, initially, a leftward-propagating bow shock wave emerges ahead of the step. This shock wave undergoes multiple reflections on both the upper and lower walls, with the two shock-wall interaction patterns located near the left side of the domain transitioning from regular to Mach reflection. Additionally, due to over-expansion, the gas around the corner interacts with the step surface and generates a weak isolated oblique shock wave that eventually intersects with multiple reflected shock waves.

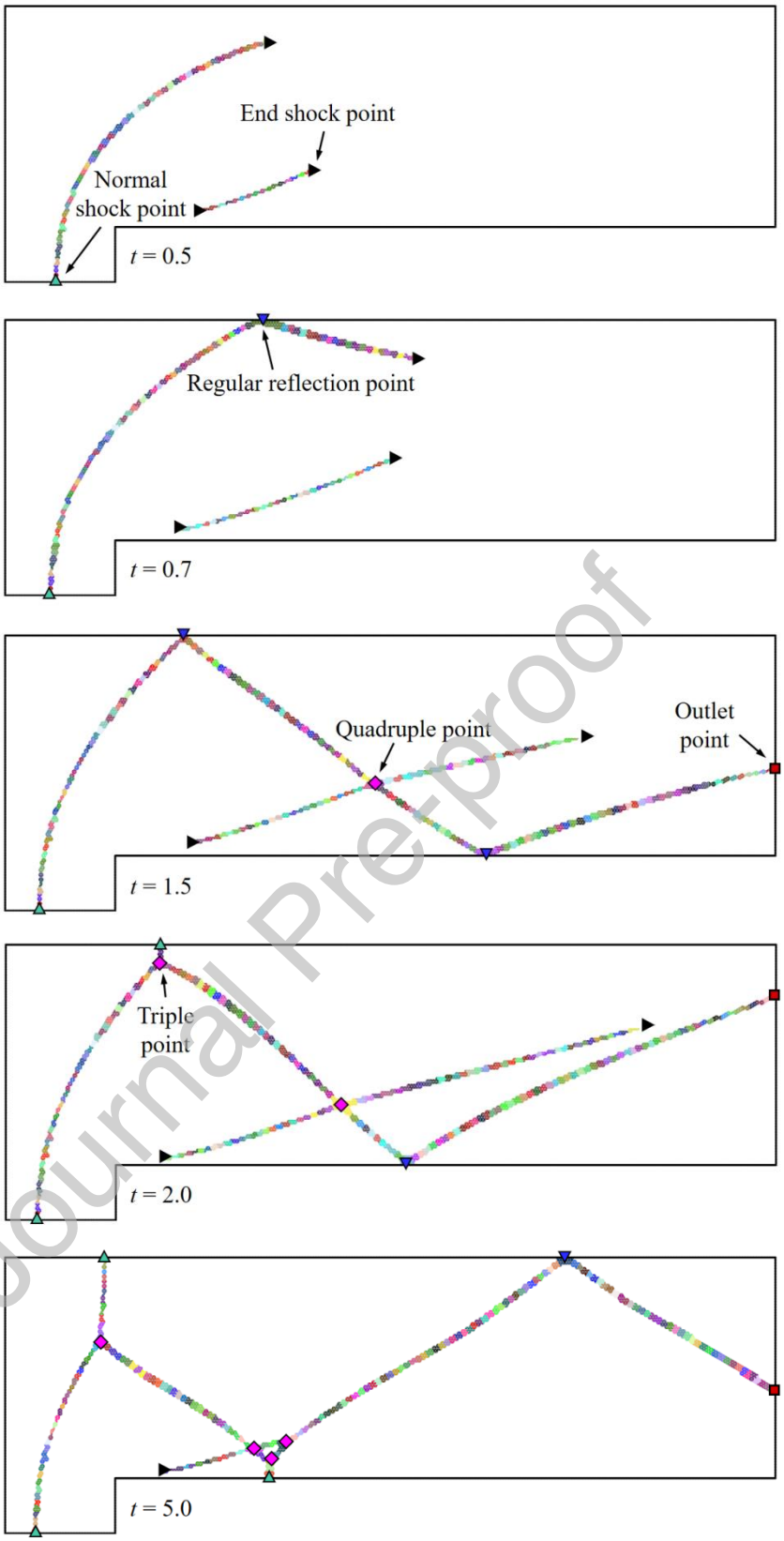

Fig. 31. Forward-facing step problem: the post-merge clustering results of shock-cells at five different moments

Although the shock waves in this problem are constantly moving and deforming, accompanied by intricate intersections and reflections, the strategy described in Sect. 2.1 effectively identifies the shock-cells. Fig. 31 shows the post-merged clustering results of the detected shock-cells at five

critical moments during the computation. Initially, two isolated shock waves, a normal shock point ahead of the step, and three end shock points are identified at time $t = 0.5$. Subsequently, a regular reflection point on the upper wall is detected at $t = 0.7$, indicating a regular shock-wall reflection in the flow field. As the computation proceeds, the quadruple point, outlet point, and triple point are sequentially identified, clearly displaying the shock wave patterns at various moments. At termination time $t = 5$, ten key shock points (i.e., three normal shock points, three triple points, one quadruple point, one end shock point, one regular reflection point, and one outlet point) are automatically identified to establish the topological structure of the shock wave configuration.

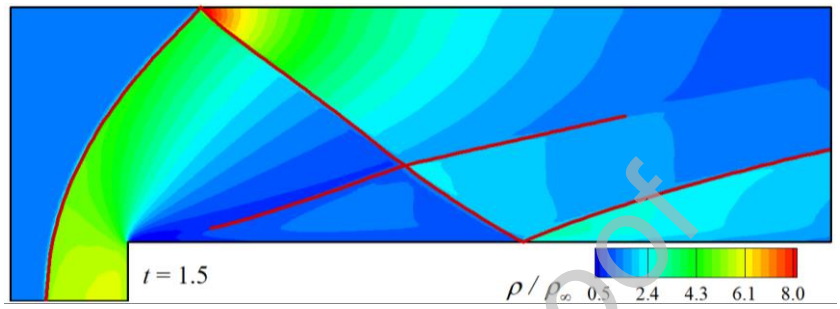

(a)

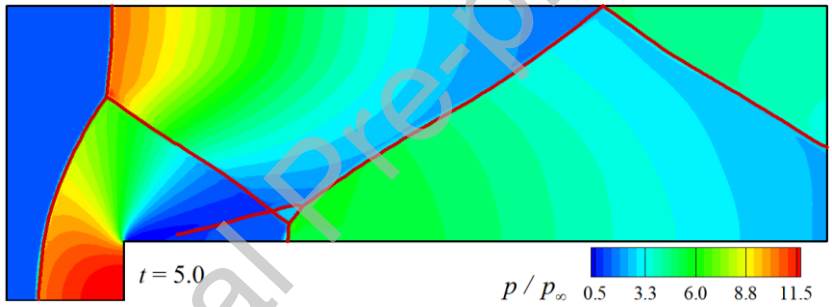

(b)

Fig. 32. Forward-facing step problem: (a) the comparison between detected shock-lines and density iso-contours at $t = 1.5$, (b) the comparison between detected shock-lines and pressure iso-contours at $t = 5.0$

The comparisons between the final detected shock-lines and the shock-capturing solutions at two moments $t = 1.5$ and $t = 5.0$, as depicted in Fig. 32, demonstrate a strong agreement between the detection results of both approximately straight shock waves and curved bow shock wave with their captured counterparts. This indicates that the proposed method exhibits excellent reliability for various shapes of moving shock waves. Moreover, visualizing these detected shock-lines in a single figure facilitates an analysis of the evolution process of shock waves and enhances our understanding of interactions among moving shock waves. As shown in Fig. 33, the Mach reflection occurs earlier near the upper wall compared to near the surface of the step. After the moment $t = 1.5$, while the bow shock wave moves slowly, there is a relatively rapid downward sliding motion observed for the triple point along this bow shock wave. The oblique shock wave induced by the rarefaction fan at the corner exhibits negligible displacement during the computation.

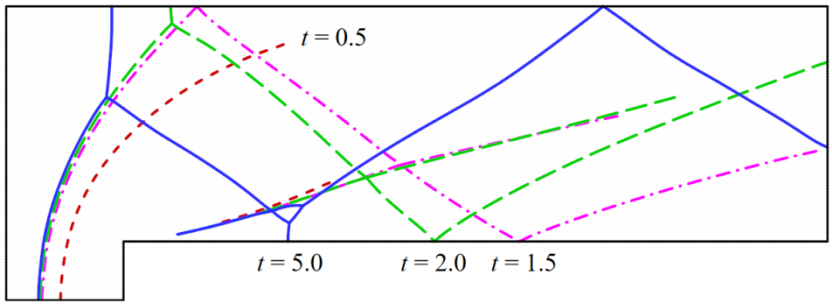

Fig. 33. Forward-facing step problem: the comparison of shock-lines detected at four different moments

4. Conclusions

Compared to conventional shock wave detection methods, the method proposed in this paper can automatically identify the shock wave patterns in two-dimensional inviscid steady and unsteady compressible flows. First, a shock wave detection algorithm based on the local flow variables is performed to extract the grid-cells characterizing the locations of shock waves. Subsequently, the *K*-means clustering algorithm and a set of well-defined strategies are utilized to accurately determine multiple shock interaction points. Finally, the Bézier curve fitting algorithm is applied to obtain high-quality shock-lines. Several numerical test cases demonstrate that the recognition accuracy of shock-line positions is generally unaffected by the computational grid scale. For both interaction points induced by the shock waves on the same side and bending shock waves, the detection accuracy may be slightly influenced by the resolution of captured shock waves. Thus, for complex flows, more accurate detection results can be obtained by using refined grids. This method offers a high degree of automation and is applicable to any grid type, ensuring reliable and accurate identification of moving shock waves in complex unsteady flows.

Given its ability to effectively identify accurate shock wave patterns, this globally-oriented shock wave detection method holds great potential for various flow study techniques that require accurate localization of shock waves, such as shock-fitting methods [21-25], adaptive grid refinement [33], and flow visualization [34]. Moreover, this method can be easily extended to detect three-dimensional individual shock wave (e.g., the bow shock wave ahead of a blunt body). On the other hand, for complex three-dimensional shock interaction structures, the idea of tomographic reconstruction can be employed to decompose the flow field into a series of two-dimensional slices. Thus, the proposed method in this paper enables identification of shock wave patterns on each slice and facilitates recognition of three-dimensional shock wave patterns. The preliminary attempts about three-dimensional shock wave pattern recognition can be found in [35]. Furthermore, directly extending the method proposed in this paper to three-dimensional flows poses a significant challenge. This is due to the fact that the strategy for classifying shock-clusters relies on counting the number of neighboring clusters, which is not effective in three-dimensions. For instance, a

shock-cluster could have more than four neighboring clusters and be located indiscriminately on a boundary, shock surface, or triple point. Consequently, it is not feasible to identify the shock wave pattern solely based on the number of neighboring clusters. Therefore, an alternative strategy must be explored for the recognition of shock wave patterns in three-dimensions.

Authorship contribution statement

Siyuan Chang: Term, Conceptualization, Methodology, Software, Formal analysis, Investigation, Resources, Writing - Original Draft, Writing - Review & Editing. **Jun Liu:** Software, Validation, Investigation, Writing - Review & Editing, Visualization. **Kai Cui:** Resources, Visualization, Supervision, Project administration.

Acknowledgments

This work has been supported and sponsored by the National Natural Science Foundation of China (No. U21B2054) and the Basic frontier science research program of Chinese Academy of Sciences (No. ZDBS-LY-JSC005).

Declaration of competing interest

The authors declare that they have no known competing financial interests or personal relationships that could have appeared to influence the work reported in this paper.

Data availability

Data will be made available on request.

References

[1] Z.N. Wu, Y. Xu, W. Wang, et al., Review of shock wave detection method in CFD post-processing, Chinese Journal of Aeronautics 26(3) (2013) 501-513. https://doi.org/10.1016/j.cja.2013.05.001.

[2] P. Buning, J. Steger, Graphics and flow visualization in computational fluid dynamics, 7th Computational Physics Conference. (1985) 1507.

[3] D.L. Darmofal, Hierarchal visualization of three-dimensional vortical flow calculations, Cambridge: Massachusetts Institute of Technology Cambridge Computational Fluid Dynamics Lab. (1991) 42-43.

[4] S.P. Liou, A. Singh, S. Mehlig, et al, An image analysis based approach to shock identification in CFD, 33rd Aerospace Sciences Meeting and Exhibit. (1995) 117.

[5] D. Lovely, R. Haimes, Shock detection from computational fluid dynamics results, 14th Computational Fluid Dynamics Conference. (1999) 3285.

[6] H.G. Pagendarm, B. Seitz, An algorithm for detection and visualization of discontinuities in scientific data fields applied to flow data with shock waves. III. Eurographics Workshop in Visualization in Scientific Computing, Viareggio, Italy, (1992).

[7] J. Van Rosendale, Floating shock fitting via Lagrangian adaptive meshes, NASA conference publication. NASA. (1995) 127-138.

[8] K.L. Ma, J. Van Rosendale, W. Vermeer, 3D shock wave visualization on unstructured grids, Proceedings of 1996 Symposium on Volume Visualization. (1996) 87-94.

[9] M. Kanamori, K. Suzuki, Shock wave detection in two-dimensional flow based on the theory of characteristics from CFD data, Journal of Computational Physics. 230(8) (2011) 3085-3092. https://doi.org/10.1016/j.jcp.2011.01.007.

[10] M. Kanamori, K. Suzuki, Three-dimensional shock wave detection based on the theory of characteristics, AIAA Journal. 51(9) (2013) 2126-2132. https://doi.org/10.2514/1.J051922.

[11] M. Monfort, T. Luciani, J. Komperda, et al., A deep learning approach to identifying shock locations in turbulent combustion tensor fields. Modeling, Analysis, and Visualization of Anisotropy. Springer International Publishing. (2017) 375-392.

[12] Y. Liu, Y.T. Lu, Y.Q. Wang, et al., A CNN-based shock detection method in flow visualization, Computers & Fluids. 184 (2019) 1-9. https://doi.org/10.1016/j.compfluid.2019.03.022.

[13] C. Liu, R. Jiang, D. Wei, et al., Deep learning approaches in flow visualization, Advances in Aerodynamics. 4(1) (2022) 1-14. https://doi.org/10.1186/s42774-022-00113-1.

[14] I.A. Doroshchenko, I.A. Znamenskaya, N.N Sysoev, et al., High-speed flow structures detection and tracking in multiple shadow images with matching to CFD using convolutional neural networks, Scientific Visualization. 14 (2022) 1-11. https://doi.org/10.26583/sv.14.4.01.

[15] H. Chen, Y. Tian, M. Guo, et al., Flow field reconstruction and shock train leading edge position detection of scramjet isolation section based on a small amount of CFD data, Advances in Aerodynamics. 4(1) (2022) 1-15. https://doi.org/10.1186/s42774-022-00121-1.

[16] N.T. Smith, M.J. Lewis, R. Chellappa, Extraction of oblique structures in noisy schlieren sequences using computer vision techniques, AIAA Journal. 50 (2012) 1145–1155. https://doi.org/10.2514/1.J051335.

[17] H. Akhlaghi, A. Daliri, M.R. Soltani, Shock-wave-detection technique for high-speed rarefied-gas flows, AIAA Journal. 55(11) (2017) 3747-3756. https://doi.org/10.2514/1.J055819.

[18] T.R. Fujimoto, T. Kawasaki, K. Kitamura, Canny-edge-detection/Rankine-Hugoniot-conditions unified shock sensor for inviscid and viscous flows, Journal of Computational Physics. 396 (2019) 264–279. https://doi.org/10.1016/j.jcp.2019.06.071.

[19] G. Li, K. Kontis, Z. Fan, Automatic shock detection, extraction, and fitting in schlieren and shadowgraph Visualization, AIAA Journal. 59 (2021) 2312–2317. https://doi.org/10.2514/1.J059667.

[20] R. Paciorri, A. Bonfiglioli, Accurate detection of shock waves and shock interactions in two-dimensional shock-capturing solutions, Journal of Computational Physics. 406 (2020) 109196. https://doi.org/10.1016/j.jcp.2019.109196.

[21] R. Paciorri, A. Bonfiglioli, A shock-fitting technique for 2D unstructured grids, Computers & Fluids. 38(3) (2009) 715-726. https://doi.org/10.1016/j.compfluid.2008.07.007.

[22] D.Y. Zou, C.G. Xu, H.B. Dong, et al., A shock-fitting technique for cell-centered finite volume methods on unstructured dynamic meshes, Journal of Computational Physics. 345 (2017) 866-882. https://doi.org/10.1016/j.jcp.2017.05.047.

[23] S.Y. Chang, X.Z. Bai, D.Y. Zou, et al., An adaptive discontinuity fitting technique on unstructured dynamic grids, Shock Waves. 29 (2019) 1103-1115. https://doi.org/10.1007/s00193-019-00913-3.

[24] A. Assonitis, R. Paciorri, M. Ciallella, et al., Extrapolated shock fitting for two-dimensional flows on structured grids, AIAA Journal. 60(11) (2022) 6301-6312. https://doi.org/10.2514/1.J061893.

[25] M. Ciallella, M. Ricchiuto, R. Paciorri, et al., Extrapolated discontinuity tracking for complex 2D shock interactions, Computer Methods in Applied Mechanics and Engineering. 391 (2022) 114543. https://doi.org/10.1016/j.cma.2021.114543.

[26] F. Zhang, J. Liu, B.S. Chen, Modified multi-dimensional limiting process with enhanced shock stability on

unstructured grids, Computers & Fluids. 161 (2018) 171–188. https://doi.org/10.1016/j.compfluid.2017.11.019.

[27] B. Everitt, T. Hothorn, An introduction to applied multivariate analysis with R, Springer New York Dordrecht Heidelberg London. (2011) 225. https://doi.org/10.1007/978-1-4419-9650-3.

[28] A. Likas, N. Vlassis, J.J. Verbeek, The global K-means clustering algorithm, Pattern Recognition. 36(2) (2003) 451-461. https://doi.org/10.1016/S0031-3203(02)00060-2.

[29] S.S. Khan, A. Ahmad, Cluster center initialization algorithm for K-means clustering, Pattern Recognition Letters. 25(11) (2004) 1293–1302. https://doi.org/10.1016/j.patrec.2004.04.007.

[30] L.J. Shao, H. Zhou, Curve fitting with Bezier cubics, Graphical models and image processing. 58(3) (1996) 223-232. https://doi.org/10.1006/gmip.1996.0019.

[31] A.N. Lyubimov, V.V. Rusanov, Gas flows past blunt bodies, part II: table of the gasdynamic functions. NASA. TT, F-715 (1973).

[32] S. Tu, S. Aliabadi, A slope limiting procedure in discontinuous Galerkin finite element method for gasdynamics applications, International Journal of Numerical Analysis and Modeling. 2(2) 2005 163-178.

[33] F. Alauzet, A. Loseille, A decade of progress on anisotropic mesh adaptation for computational fluid dynamics, Computer-Aided Design. 72 (2016) 13-39. https://doi.org/10.1016/j.cad.2015.09.005.

[34] A.J. Smits, Flow visualization: techniques and examples. World Scientific. (2012).

[35] M.N. Lin, Z.W. Tian, S.Y. Chang, et al., Three-dimensional shock topology detection method via tomographic reconstruction, Aerospace. 10(3) (2023) 275. https://doi.org/10.3390/aerospace10030275.

Declaration of interests

☒The authors declare that they have no known competing financial interests or personal relationships that could have appeared to influence the work reported in this paper.

☐The authors declare the following financial interests/personal relationships which may be considered as potential competing interests: